J. Fluid Mech. (2013), *vol.* 726, *pp.* 559–595. © Cambridge University Press 2013
doi:10.1017/jfm.2013.244

Horizontal convection dynamics: insights from transient adjustment

Ross W. Griffiths†, Graham O. Hughes and Bishakhdatta Gayen

Research School of Earth Sciences, Australian National University, Canberra, ACT 0200, Australia

(Received 16 December 2012; revised 26 March 2013; accepted 9 May 2013;
first published online 11 June 2013)

The dynamics of horizontal convection are revealed by examining transient adjustment toward thermal equilibrium. We restrict attention to high Rayleigh numbers (of $O(10^{12})$) and a Prandtl number ~ 5 that characterize many practical applications, and consider responses to small changes in the thermal boundary conditions, using laboratory experiments, three-dimensional direct numerical simulations (DNS) and simple theoretical models. The experiments and the mechanical energy budget from the DNS demonstrate that unsteady forcing can produce flow dramatically more active than horizontal convection under steady forcing. The physical mechanisms at work are indicated by the time scales of approach to the new equilibrium, and we show that these can range over two orders of magnitude depending on the imposed change in boundary conditions. Changes that lead to a net destabilizing buoyancy flux give rapid adjustments: for applied heat flux conditions the whole of the circulation is controlled by conduction through the stable portion of the boundary layer, whereas for applied temperature difference the circulation is controlled by small-scale convection within the unstable part of the boundary layer. The experiments, DNS and models are in close agreement and show that the time scale under applied temperatures is as small as 0.01 vertical diffusion time scales, a factor of four smaller than for imposed flux. Both cases give adjustments too rapid for diffusion in the interior to play a significant role, at least through 99 % of the adjustment, and we conclude that diffusion through the full depth is not significant in setting the equilibrium state. Boundary changes leading to a net stabilizing buoyancy flux give a very different response, causing the convection to quickly form a shallow circulation cell, followed eventually by a return to full-depth overturning through a combination of penetrative convection and conduction. The time scale again varies by orders of magnitude, depending on the boundary conditions and the location of the imposed boundary perturbation.

Key words: convection, convection in cavities, ocean circulation

1. Introduction

Convection forced by a variation in temperature or heat flux along one horizontal boundary has been studied for its relevance to large-scale ocean circulation, lake circulation and industrial processes (Stommel 1962; Rossby 1965, 1998; Mullarney, Griffiths & Hughes 2004; Wang & Huang 2005; Chiu-Webster, Hinch & Lister 2008; Hughes & Griffiths 2008). Whereas Rayleigh–Bénard convection is used

† Email address for correspondence: Ross.Griffiths@anu.edu.au

https://doi.org/10.1017/jfm.2013.244 Published online by Cambridge University Press

as the archetypical, idealized case for flow under differential heating between two horizontal boundaries and assumes horizontally uniform boundary conditions, horizontal convection is the canonical case for heat flow through a single boundary. However, studies of horizontal convection have focused on the time-averaged, thermally equilibrated state under steady boundary conditions, a special case in which the flow gives no net vertical heat transport through the forcing boundary or through any level in the fluid. At large Rayleigh numbers ($Ra \gtrsim 10^{10}$, where Ra is appropriately based on the horizontal length) this flow involves a thermal boundary layer that is purely conductive over a part of the forcing boundary but which encompasses an unstable, convecting sublayer over the region of destabilizing buoyancy flux. A vertical plume (at the end of the box in the case of a monotonic boundary temperature distribution) connects the boundary layer flow to the bulk of the domain, and the circulation closes through a widespread vertical advection (outside the plume) toward the forcing boundary (see Gayen *et al.* 2013, and online movies available at http://dx.doi.org/10.1017/jfm.2013.244).

This thermally equilibrated state represents a fine balance in which the buoyancy becomes sufficient to force vertical flow (in the plume) out of the boundary layer only against the endwall. Heat is carried from the heated to the cooled region of the boundary and buoyancy is transported through the plume and interior (Hughes & Griffiths 2008). In mechanical energy terms this equilibrium state is dominated by an approximate balance between production of kinetic energy from available potential energy in the plume and the reverse in the interior of the volume (Whitehead & Wang 2008; Gayen *et al.* 2013), with remarkably little dissipation (Scotti & White 2011; Gayen *et al.* 2013). The flow also achieves an exact balance between the rates of generation of available potential energy at the boundary and of irreversible mixing (Hughes, Hogg & Griffiths 2009; Gayen *et al.* 2013). However, the equilibrium state is a special case that may not be reached in many practical situations. This state also offers only relatively limited access to information about the flow dynamics. A full understanding of horizontal convection, including the equilibrium state, needs to consider the approach to thermal equilibrium and the transient adjustments after changes in the boundary forcing. The transient flows are a subset of more general cases that have a net vertical heat transport.

The response to changes in thermal boundary conditions is itself of particular interest in the very important task of understanding the ocean overturning circulation and its response to climatic changes of the surface buoyancy conditions. The density differences in the oceans can be produced only by buoyancy fluxes across the sea surface (neglecting geothermal heat input at the sea floor and small contributions arising from internal energy conversions via the nonlinear equation of state). Hence, the time required for the ocean to equilibrate to changes in surface thermal conditions, and also the computational time required for ocean models to equilibrate, are largely determined by the rate of adjustment of the stratification, for which the idealized case of horizontal convection (without surface wind stress) gives relevant insights. Indeed, ocean modelling is providing evidence that the surface buoyancy forcing provides a substantial fraction of the power input to the ocean circulation (Borowski, Gerdes & Olbers 2002; Hogg 2010; Saenz *et al.* 2012). The adjustment time scale for the ocean, and of pure horizontal convection, has commonly been assumed to be of the order of the time for diffusion (whether molecular or turbulent) through the depth of the domain: a very long time for geophysical and large industrial cases. The question also arises as to whether there is a threshold amplitude for surface boundary perturbations that could cause a shut down of the deep, high-latitude sinking, as suggested by ocean

https://doi.org/10.1017/jfm.2013.244 Published online by Cambridge University Press

models with increased freshwater buoyancy input at high latitude (e.g. Ganopolski & Rahmstorf 2001). It would be relevant to know what the threshold is in a purely buoyancy-forced overturning.

There has not been a systematic study of the adjustment mechanisms and time scales in horizontal convection. Two-dimensional numerical solutions at modest Rayleigh numbers in a square box (up to $Ra = 10^8$; Rossby 1998) illustrate responses to changes in the imposed distribution of temperature along the base of the box, with a 'fast path' for changes to propagate within the boundary layer and a 'slow path' through the interior. The fast path was evident when a perturbation was imposed at the cooling thermal boundary and the response was advected along the boundary layer, whereas the slow path was required when the perturbation was imposed at the heating end of the base, thereby directly altering the plume and propagating through the interior. For an increase in heating temperature (giving a net heat input and warming of the box) there was a period of more rapid overturning, whereas for a decrease in heating (a net cooling of the box) there was a period of shallow convection followed by a slow return to full-depth convection. Similar qualitative observations of either a period of increased overturning or the formation of a shallow cell have been reported in laboratory experiments and two-dimensional numerical solutions up to $Ra \sim 10^{12}$ (Mullarney *et al.* 2004). Here we shall show that the slow interior path characterizes the internal adjustment and equilibration, for all boundary perturbations that lead to a non-zero net heat flux through the boundary, hence to a change in the total heat content of the box.

The nature of non-equilibrium flow and its role in establishing equilibrium states is further illustrated by experiments in which horizontal convection was forced by an oscillatory boundary heating in a see-saw pattern, with the heating applied to two regions near the ends of a basin and each heat flux oscillating out of phase with the other (Griffiths, Maher & Hughes 2011). This arrangement is somewhat like the seasonal cycle of thermal forcing to the oceans: the time-averaged interior temperature, which is most strongly influenced by phases of maximum heating at one end or the other, was found to be is dependent on the externally imposed forcing period relative to internal adjustment time scales.

In previous studies, ranging from the early experiments of Rossby (1965) to recent developments in three-dimensional direct numerical simulations (DNS) (Scotti & White 2011), the equilibration process has largely been an annoyance in achieving equilibrium states. Fortunately, the reported equilibration times have consistently been an order of magnitude less than the diffusion time through the depth of the box (in the upper range of Rayleigh numbers examined), but the surprisingly short times have not been explained. In experiments with convection forced by salt and freshwater buoyancy (Pierce & Rhines 1996; Whitehead & Wang 2008; Stewart, Hughes & Griffiths 2012) the Rayleigh number is very large and equilibrium states were reached within a day, yet the time scale for molecular diffusion of salt through the depth of the box is many years. In ocean circulation modelling, where buoyancy conditions are applied at the ocean surface so that horizontal convection contributes in some part to the large-scale flow, the model equilibration times are again found to at least an order of magnitude shorter than the time scale for diffusion through the ocean depth given the specified turbulent diffusivity. The current study resolves the question of equilibration time scale by highlighting which mechanisms of vertical transport are important in horizontal convection, something that studies of equilibrium states have been unable to demonstrate.

https://doi.org/10.1017/jfm.2013.244 Published online by Cambridge University Press

Here we examine the transient flows and internal adjustment time scales following various kinds of imposed instantaneous changes in the thermal boundary conditions. We use conditions similar to those in previous experiments with equilibrium states (in particular, large Rayleigh number, small aspect ratio and piecewise uniform boundary conditions). In § 2 we present theoretical predictions of the adjustment times for destabilizing changes in boundary conditions, under either imposed temperature difference or imposed flux conditions, and with changes applied in either the heated or the cooled region of the boundary. In § 3 we report laboratory experiments with small step changes to the thermal boundary conditions, and in § 4 describe the transient flows in terms of the evolution of the temperature field. In § 5 we make use of three-dimensional DNS designed to capture the transient flows, complementing the experiments for a number of key cases. The same DNS have been discussed previously in the context of the mechanical energy budget of the equilibrated state (Gayen *et al.* 2013), but here we utilize the transient solutions. In § 6 we bring together information on the adjustment times for all cases and show that adjustment can be very rapid compared with diffusion of buoyancy through the depth of the domain, and that applied temperature difference and applied heat flux cases are very different, in line with the theoretical predictions for different controlling mechanisms.

2. Theoretical hypotheses

Consider the case of convection that is initially at thermal equilibrium under a given steady thermal forcing at the base. A small step change (which we refer to as a boundary perturbation) is then made in either the heating or the cooling boundary condition, and the flow proceeds to adjust, as does the average temperature in the box. For simplicity, we assume a rectangular box (of length L, width W and depth D) heated over one half of the base and cooled over the other half in a piecewise uniform fashion (Mullarney *et al.* 2004; Stewart, Hughes & Griffiths 2011), density differences everywhere outside the boundary layer that are very small compared with the applied temperature difference, and an adjustment time that is long compared to the time taken to recycle the box volume through the boundary layer (the ventilation time scale).

The equilibrium convection is characterized by either the Rayleigh or the flux Rayleigh number (depending on the boundary conditions),

$$Ra \equiv \frac{\alpha g \Delta T L^3}{\nu\kappa}, \quad Ra_F \equiv \frac{g\alpha F L^4}{\rho_0 c_p \nu \kappa^2}, \tag{2.1}$$

where $\Delta T = T_H - T_C$ is the applied temperature difference, F is the input heat flux (per unit area) over the heated portion of the base, and fluid properties are the specific heat capacity c_p, the kinematic viscosity ν, the thermal diffusivity κ and the reference density ρ_0. In the following we make use of established scaling results for the boundary layer streamfunction, ψ_{bl} and thickness, h, for the cases of applied temperature (Rossby 1965),

$$\psi_{bl}/\kappa \approx c_1 Ra^{1/5}, \quad h/L \approx c_2 Ra^{-1/5}, \tag{2.2}$$

or applied flux (Mullarney *et al.* 2004),

$$\psi_{bl}/\kappa \approx c_1 Ra_F^{1/6}, \quad h/L \approx c_2 Ra_F^{-1/6}. \tag{2.3}$$

The numerical factors are in both cases $c_1 \approx 1.0$ and $c_2 \approx 2.7$ (Hughes *et al.* 2007). Note that the Rayleigh number is based on the horizontal length L over which the thermal forcing is imposed. The time scale consistent with this choice is L^2/κ.

https://doi.org/10.1017/jfm.2013.244 Published online by Cambridge University Press

However, the dimensionless time $\hat{t}_D = \kappa t/D^2$ will generally be used in the following analysis and report of experimental results.

2.1. *Warming under an imposed heating flux*

In cases with imposed heating flux, the initial state has an interior temperature T_1 and a total heat input $Q_1 (\equiv F_1 WL/2)$ through the heated half of the base, whereas a fixed temperature T_C is applied over the cooling half of the base. The cooled boundary layer is stable and the rate of heat withdrawal from the box at any time is determined by conduction through the boundary layer thickness h. In the initial steady state the flux withdrawn is equal to the input Q_1. In the first class of boundary perturbation to be considered, the heat input is increased at time $t = 0$ from Q_1 to $Q_2 = Q_1 + \delta Q$. Previous experiments and numerical solutions show that the boundary buoyancy input in the equilibrium state is carried to the top of the box by the endwall plume (Mullarney *et al.* 2004; Stewart *et al.* 2011; Gayen *et al.* 2013). Thus, we can assume that in the transient flow the 'unbalanced' buoyancy input (in excess of that in the equilibrium state) will also be carried to the top of the box by the plume, where it spreads laterally across the top of the box before being displaced downward by the continuing plume transport. Hence, the interior temperature $T(t)$ proceeds to increase, leading to an increasing temperature difference $T - T_c$ across the boundary layer and an increasing rate of conductive heat withdrawal, which we write as $Q = Q_1 + Q'(t)$. The rate of change of temperature $\bar{T}$ averaged over the interior (assuming $h \ll D$) is given by the heat transport imbalance

$$\rho_0 c_p DLW \frac{\mathrm{d}\bar{T}}{\mathrm{d}t} = \delta Q - Q'(t). \tag{2.4}$$

The imbalance vanishes at large times, when $Q' \to \delta Q$. For quasi-steady conduction in the boundary layer over the cooled half of the base, the rate of heat withdrawal is

$$Q_1 + Q'(t) \approx \beta \rho_0 c_p \kappa (\bar{T} - T_C) LW/2h, \tag{2.5}$$

where we allow for cooling over length $L/2$ and write the gradient at the boundary as $\mathrm{d}T/\mathrm{d}z \approx \beta(\bar{T} - T_C)/h$. When h is defined such that 95 % of the overall temperature difference lies in the boundary layer, the constant evaluated from DNS is $\beta \approx 1.4$. At large time the system approaches the final equilibrium state, in which $\bar{T} = T_2$ and

$$Q_1 + \delta Q \approx \beta \rho_0 c_p \kappa (T_2 - T_C) LW/2h. \tag{2.6}$$

Taking h as constant for small changes in boundary conditions and combining (2.4)–(2.5) gives the interior temperature

$$\bar{T} \approx T_1 + \delta T(1 - \mathrm{e}^{-\beta\kappa t/2hD}), \tag{2.7}$$

which exponentially approaches a final equilibrium temperature T_2, the magnitude of the resulting change being

$$\delta T = T_2 - T_1 = 2h\delta Q/(\beta \rho_0 c_p \kappa LW) = h\delta F/(\beta \rho_0 c_p \kappa). \tag{2.8}$$

In normalized form, the deviation from the final equilibrium is

$$\Theta = (\bar{T} - T_2)/(T_1 - T_2) \approx \mathrm{e}^{-\beta\kappa t/2hD}. \tag{2.9}$$

The imposed flux condition causes the box to equilibrate to the new conditions on the exponential time scale $\tau_F \approx 1.4hD/\kappa$. The Rayleigh number scaling (2.3) justifies

https://doi.org/10.1017/jfm.2013.244 Published online by Cambridge University Press

our assumption of constant h for modest changes in boundary conditions. It also implies more rapid adjustment for larger Ra_F:

$$\kappa\tau_F/D^2 \approx (2/\beta)(h/D) \approx (2c_2/\beta)A^{-1}Ra_F^{-1/6}, \tag{2.10}$$

where $A = D/L$ is the aspect ratio of the box. Under the conditions of the experiments reported in this paper we will find $\kappa\tau_F/D^2 \approx 0.1$ (or $\tau_F \approx 2 \times 10^4$ s).

The above argument carries over to a second class of boundary perturbations: the case of a small increase in the cooling boundary temperature T_C in the presence of a fixed heating flux. In this case the boundary perturbation causes the conductive heat withdrawal to be temporarily reduced. The boundary layer water is then warmer when it reaches the heating region of the base, where the imposed heat input drives more vigorous instability and stronger mean circulation.

Thus, for net warming cases with applied heat flux, we hypothesize that the equilibration time is determined by conductive heat loss across the stable boundary layer and the heat capacity of the box. In this model diffusion down vertical gradients in the bulk of the fluid plays a negligible role because the interior gradients are both very small and remain unchanged between equilibrium states for small boundary changes, whereas vertical advection of heat and buoyancy in the plume is far more efficient. The model does not rule out a slower diffusive adjustment in the interior. However, it is likely that such a diffusive response will be a very small component of the overall adjustment, and smaller than the amplitude of fluctuations in the equilibrium state. Such an unimportant contribution will be a challenge to detect.

Recall that we have assumed an adjustment time much longer than the ventilation time, because the plume transport to the top causes a non-uniform warming in the interior in the initial stages of the transient flow. The ventilation time based on the boundary layer transport alone is $t_V \sim (LD)/\psi_{bl}$, or using (2.3), $\kappa t_V/D^2 \sim (c_1A)^{-1}Ra_F^{-1/6}$. Hence the ratio of time scales $\tau_F/t_V \approx 2c_1c_2/\beta \approx 3.9$ is a constant, independent of both Rayleigh number and aspect ratio, and our assumption holds.

2.2. *Warming under imposed temperatures*

A third class of boundary perturbation is again net warming owing to an increase in the heating temperature, but under an applied temperature difference. The initial state has heating boundary temperature T_{H1} and average interior temperature T_1, whereas the final state has heating temperature $T_{H2} = T_{H1} + \delta T$ and interior at T_2. The cooling boundary temperature is held constant at T_C. In this case we have no direct information about the heat flux during transient flow. Neglecting the volume of the thin boundary layer, the interior temperature $\bar{T}(t)$ warms according to the difference between heat input Q_H and cooling Q_C:

$$\rho_0 c_p DLW\frac{\mathrm{d}\bar{T}}{\mathrm{d}t} = Q_H - Q_C. \tag{2.11}$$

We write the heat input to the interior as that carried out of the boundary layer by the plume,

$$Q_H(t) \approx \rho_0 c_p W\psi_{bl}(T_{H2} - \bar{T}), \tag{2.12}$$

and write the corresponding cooling flux in the same form as the right-hand side of (2.5) but with an additional prefactor γ that represents the fraction of the total heat or buoyancy flux (in the equilibrium states) leaving the boundary layer in the plume:

$$Q_C(t) \approx \gamma\beta\rho_0 c_p\kappa(\bar{T} - T_C)LW/2h. \tag{2.13}$$

https://doi.org/10.1017/jfm.2013.244 Published online by Cambridge University Press

The heat budget (2.11) becomes

$$DL\frac{\mathrm{d}\bar{T}}{\mathrm{d}t} \approx \psi_{bl}(T_{H2} - \bar{T}) - \gamma\beta\kappa(\bar{T} - T_C)L/2h, \tag{2.14}$$

where T_{H2} and T_C are fixed throughout the adjustment ($t > 0$). Both h and ψ_{bl} are also taken as constant for small boundary temperature changes.

In the large time thermal equilibrium state, the time-dependence vanishes and $\bar{T} = T_2$, the final interior temperature, so that (2.14) gives

$$\frac{(T_{H2} - T_2)}{(T_2 - T_C)} \approx \frac{\gamma\beta\kappa L}{2h\psi_{bl}} \approx \frac{\gamma\beta}{2c_1c_2}, \tag{2.15}$$

where the scaling (2.2) is used in the final step. Thus, the temperature at the top of the box in the equilibrium state, normalized by $\Delta T = T_{H2} - T_C$, is a constant,

$$\hat{T}_{top} \equiv \frac{T_2 - T_C}{\Delta T} \approx \frac{2c_1c_2}{2c_1c_2 + \gamma\beta}. \tag{2.16}$$

Given $\beta \approx 1.4$ (from DNS, Gayen *et al.* 2013), $\gamma \approx 0.14$ (from a steady-state theoretical solution, Hughes *et al.* 2007) and the values of the prefactors in (2.2), $\hat{T}_{top} \approx 0.96$.

Substituting the large time equilibrium solution into (2.14) leaves a homogeneous equation, which is conveniently rewritten in terms of the normalized deviation from the final equilibrium, defined as in the previous case, $\Theta = (\bar{T} - T_2)/(T_2 - T_1)$. Then

$$\frac{\mathrm{d}\Theta}{\mathrm{d}t} \approx (DL)^{-1}(\psi_{bl} + \gamma\beta\kappa L/2h)\Theta \tag{2.17}$$

and

$$\Theta \approx \exp[-(\psi_{bl}/DL + \gamma\beta\kappa/2hD)t] = \mathrm{e}^{t/\tau_\Delta}. \tag{2.18}$$

The exponential adjustment time scale is

$$\tau_\Delta = DL/\left[\psi_{bl}\left(1 + \frac{\gamma\beta}{2}\frac{L}{h}\frac{\kappa}{\psi_{bl}}\right)\right], \tag{2.19}$$

where the Rossby scaling (2.2) reduces the bracketed term in the denominator (and following (2.15)) to $[1+\gamma\beta L\kappa/(2h\psi_{bl})] = [1+\gamma\beta/2c_1c_2] \approx 1+0.04$. This indicates that conduction in the stable boundary layer (the second term on the right of (2.14)) plays a negligible role in the thermal adjustment compared to convection in the unstable, heated portion of the boundary layer. Hence, $\tau_\Delta \approx 0.96DL/\psi_{bl}$, or in normalized form

$$\kappa\tau_\Delta/D^2 \approx (0.96/c_1)A^{-1}Ra^{-1/5}. \tag{2.20}$$

Notably, under the conditions used in the experiments reported here, this time scale is two orders of magnitude smaller than the diffusion time through the depth of the box.

The ratio of the predicted time scale for imposed temperature boundary conditions to that for imposed flux (2.10) at the same value of Ra, is

$$\tau_\Delta/\tau_F \approx 0.96(\beta/2c_1c_2)c_3^{1/6} \approx 0.22, \tag{2.21}$$

where we have used $Ra_F = NuRa$ and the Nusselt number scaling for applied temperature $Nu \approx c_3Ra^{1/5}$ (Rossby 1965), where the prefactor (although not independent of the other constants) $c_3 \approx 0.48$ taken from high-Rayleigh-number DNS

https://doi.org/10.1017/jfm.2013.244 Published online by Cambridge University Press

(Gayen *et al.* 2013). The difference in time scales can be viewed as a result of a substantially thinner conduction sublayer thickness on the heating boundary compared to the full boundary layer thickness h over the cooling region.

A fourth class of boundary perturbation giving net warming again has imposed boundary temperatures, but this time the cooling temperature T_C is increased. The cold boundary layer will immediately be warmer and on arrival at the heated region of the boundary, there will be greater convective instability. Through this response to temperature changes the convective mixed layer will again control the net heat flux into the box. The analysis given above again applies (at times beyond the very short period for boundary layer advection along the base) and we predict the same response as for an increase in T_H.

2.3. *Cooling adjustments*

When the boundary perturbation is in the opposite sense, causing a net stabilizing buoyancy input and cooling, convection is suppressed. Previous work shows that a shallow convection cell is formed, with a relatively stagnant region above (Rossby 1998; Mullarney *et al.* 2004). Thus, it will be useful for interpreting the results in § 6 to consider the limiting case of conduction in a two-dimensional rigid slab with uniform initial temperature $\hat{T}_0$, boundary temperature $\hat{T} = 0$ at $z = D - d$ and insulating boundary at $z = D$, where $d < D$ and is the thickness of stagnant fluid. The temperature is accurately described by (Carslaw & Jaeger 1959, p. 96)

$$\hat{T} = \frac{4\hat{T}_0}{\pi} \mathrm{e}^{-\pi^2 \kappa t/4d^2} \sin[\pi(z + d - D)/2d] \tag{2.22}$$

at times $\kappa t/d^2 \geqslant 0.1$ and the heat flux into that volume decreases with time according to $F_d = (2\rho c_p \kappa \hat{T}_0/d)\mathrm{e}^{-\pi^2 \kappa t/4d^2}$. In the notation of (2.9) $\Theta = \hat{T}/\hat{T}_0$, at any height, and therefore Θ decreases exponentially with a time scale $(4/\pi^2)d^2/\kappa$.

Considering the question of a threshold boundary perturbation for shut down of the plume, potentially relevant quantities from the equilibrium state are the excess temperature at the heated boundary relative to the temperature in the interior, and the fraction of the gross buoyancy flux available to drive the plume beyond the boundary layer height. The scaling analysis above, for applied temperatures, predicts a normalized interior temperature (2.16) $\hat{T}_{top} = 0.96$ and DNS gives $\hat{T}_{top} = 0.95$ (Gayen *et al.* 2013). The magnitude of the excess temperature $1 - \hat{T}$ implies that a sudden decrease in T_H that reduces $\Delta T = T_H - T_C$ by more than around 5 %, will leave the boundary layer everywhere more dense than the interior density, causing the plume to shut down. For the case of applied buoyancy flux the plume buoyancy flux remaining at the edge of the boundary layer is predicted to be a fraction $\gamma \approx 14\,\%$ of the boundary input (Hughes *et al.* 2007). However, there is no direct control on boundary-layer temperature and it is not clear what magnitude of boundary flux perturbation will shut down the plume.

3. Laboratory experiments

3.1. *Apparatus*

The experiments were carried out in a rectangular box similar to that described by Mullarney *et al.* (2004) but of twice the width and with improved thermal insulation. Both changes reduce the effects of sidewall heat transfer. The internal dimensions were length $L = 1.25$ m, height $D = 200$ mm and width $W = 300$ mm. The working fluid

https://doi.org/10.1017/jfm.2013.244 Published online by Cambridge University Press

was de-aerated, demineralized water with bleach added as an antibiotic agent. Acrylic sidewalls were double-glazed with argon gas in a 20 mm gap. The acrylic lid, 75 mm thick, triple-glazed with two gaps filled with argon, was sealed within the top of the sidewalls. A minimum of 100 mm of expanded polystyrene foam was closely fitted to the lid and all sides. The base was a single copper plate, 8 mm thick. Sealed beneath one half of the copper base at one end was a heat exchanger consisting of a block of plastic machined with open channels to carry coolant water, pumped from a temperature-controlled bath. The channels were paired and interleaved, including inlets and outlets on both sides supplied by two pumps so that, when this unit was sealed against the copper plate, the coolant was in direct contact with the copper and kept the base as close as possible to a constant and uniform temperature. Beneath the other half of the base was either: (*a*) a second identical heat exchanger carrying hot water from a second water bath (giving an imposed temperature difference between the two halves of the base); or (*b*) an electrical resistance heating mat (giving an imposed, uniform heat flux through half of the base). In order to limit horizontal conductive heat transport in the copper, the heating and cooling units were separated by 50 mm of expanded foam insulation. The whole arrangement sat on expanded foam board 150 mm thick. The inner surface of the base was levelled both along and across the box to within 0.5 mm in 1000 mm.

The useful runs are summarized in table 1. The power supplied to the heating mat was controlled to within ± 0.05 W with a microprocessor-based controller (removing 3 % fluctuations in the grid electricity supply). A 'standard' power setting was $Q = 280.0$ W, giving a heat flux $F = 1556$ W m^{-2}, for which Mullarney *et al.* (2004) reported detailed measurements of the steady-state flow and two-dimensional numerical solutions. When applying a temperature difference, the temperatures were chosen to be similar to those measured in the applied flux case. For most experiments the hot water bath was held at temperatures 34.00 or 38.00 °C and the cold bath at 10.00 or 14.00 °C, to within ± 0.02 °C. In two experiments with larger heat flux ($Q = 450.0$ W, $F = 3000$ W m^{-2}) the cold bath temperature was set to 5.00 °C in order to reduce the temperature difference between the bulk of the box and the room. Further reduction of the cold temperature was undesirable given the nonlinearity of the density–temperature relation for water. Separate calorimetry experiments were used to determine the overall heat transfer coefficient for heat loss from the box to the room.

Temperature measurements were taken from eight thermistors mounted on thin support tubes, attached to a computer-driven vertical translation stage and inserted through small holes in the lid. The thermistor-bridge circuit output of 0–10 V was logged and converted to temperature through a pre-determined calibration. In some experiments the thermistors were at fixed locations, chosen to monitor key parts of the flow and periodically translated vertically to provide profiles from the top to within 3 mm of the base. In other runs the temperature was recorded only as vertical profiles taken every 2 min (at 100 and 300 mm from each end and at the midpoint of the box), from which time records at any depth could be constructed. Additional logs recorded the boundary temperatures given by four thermistors embedded in the copper base (100 mm from each end and 50 mm from each sidewall).

The room temperature was logged. One set of runs was carried out in a well-insulated laboratory with a dedicated control system giving a very stable mean room temperature of 32 °C (with a peak-to-peak range of 1.5 °C on a rapid 15 min cycle that prevents fluctuations from penetrating the insulation, and longer period fluctuations less than 0.3 °C). This was the maximum temperature available to us and the experimental conditions above were chosen such that the temperature of the bulk

https://doi.org/10.1017/jfm.2013.244 Published online by Cambridge University Press

Exp.	BC type	BC change (variable, sign)	Room (°C)	Initial BCs (W)/(°C)	Final BCs (W)/(°C)	Final T_{top} (°C)	$\kappa\tau_e/D^2$	$\kappa\tau_{95}/D^2$
1	Flux	Q warming	26	280/10.33	308/10.50	31.99	0.081	0.235
2	Flux	Q cooling	26	308/10.50	280/10.47	30.58	0.101	0.309
3	Flux	T_C warming	26	280/10.47	280/14.49	33.80	0.069	0.235
4	Flux	T_C cooling	26	280/14.49	280/10.49	30.64	0.132	0.418
5	Flux	Q warming	31.2	280/10.49	308/10.54	32.61	0.118	0.404
6	Flux	Q cooling	31.1	308/10.54	280/10.43	31.39	0.165	0.423
7	Flux	T_C warming	31.1	280/10.43	280/15.47	35.11	0.074	0.230
9	Flux	T_C cooling	31.2	280/15.47	280/10.50	29.64	0.234	0.792
10	Flux	Q warming	32.3	560/6.06	616/6.14	42.81	0.073	00.22
11	Flux	Q cooling	32.2	616/6.14	560/6.06	40.45	0.170	0.42
				(°C)/(°C)	(°C)/(°C)			
12	ΔT	T_C warming	24.9	33.75/10.63	33.83/14.58	31.83	0.025	0.083
13	ΔT	T_C cooling	24.5	33.82/14.49	33.73/10.54	31.35	0.061	0.162
14	ΔT	T_H warming	24.7	33.73/10.54	37.63/10.67	34.84	0.027	0.085
15	ΔT	T_H cooling	25.9	37.63/10.67	33.76/10.52	31.33	0.191	0.559
16	ΔT	T_H cooling	31.4	33.6/10.57	31.65/10.52	29.85		
17	ΔT	T_H warming	31.4	31.66/10.53	32.61/10.56	30.78		
18	ΔT	T_H warming	31.4	31.65/10.52	32.62/10.55	30.80		
19	ΔT	T_H cooling	31.4	32.62/10.55	31.66/10.52	30.03		
20	ΔT	T_H warming	31.4	31.66/10.52	32.14/10.53	30.41		
21	ΔT	T_H warming	31.4	32.14/10.53	36.05/10.59	33.94		
22	ΔT	T_H cooling	31.4	35.56/10.58	31.65/10.52	30.05		
23	ΔT	T_H cooling	31.4	31.6/10.5	31.1/10.5	29.6		
DNSa	ΔT	T_H warming	—	35/35	40/10	38.56	0.0175	0.0787
DNSb	ΔT	T_H warming	—	40/10	44/10	42.37	0.0175	0.0787
DNSc	ΔT	T_H cooling	—	44/10	40/10	38.72	0.21	0.75
DNSd	Flux	F Warming	—	280*/10	308*/10	39.1	0.10	0.354

TABLE 1. Summary of experimental conditions and measured adjustment times. 'Change' indicates which boundary condition (BC) is perturbed and whether the change leads to net destabilizing (warming) or net stabilizing (cooling) buoyancy input. Boundary conditions before and after the boundary perturbation are shown as (total power input Q)/(cooling temperature T_C) or (heating temperature)/(cooling temperature). Boundary temperatures for experiments were measured in the copper base 100 mm from each end, with absolute accuracies ± 0.02 °C for T_H and ± 0.10 °C for T_C. Relative accuracy of thermistors in the water is ± 0.01 °C, precision ± 0.001 °C, and standard deviations in the initial and final time averages are ± 0.004–0.008 °C. Fluxes are accurate to ± 0.1 W. (Power input of 280 W represents a heat flux 1556 W m^{-2} and corresponds to the 140 W experiments of Mullarney *et al.* (2004) in a box half the present width.) Runs 1–15, 21 and 22 have a nominal 4 °C amplitude of boundary perturbation, whether by applied flux or temperature; runs 16–20 and 23 have smaller perturbations in applied temperature T_H. Top interior temperature T_{int} and adjustment times listed here are those at $z/D = 0.875$ midway along the cooling region. For the computed solutions (DNS) quantities are given in dimensional terms in order to allow more direct comparison with the experiments; the applied power (*) is converted to the equivalent value for the width of the laboratory tank; adjustment times and T_{top} are horizontal averages at $z/D = 0.875$.

of the water in the box, at either the initial or final equilibrium state in each run, was equal to this room temperature. Another series of experiments, which serve to test the effects of sidewall heat losses, was carried out in the main fluid dynamics laboratory,

https://doi.org/10.1017/jfm.2013.244 Published online by Cambridge University Press

where the temperature was lower and had larger fluctuations (mean 26 °C, diurnal fluctuations of $+2/-0.5$ °C and 6 h cycle time).

Velocity measurements were taken in some of the experiments with applied temperature difference. These utilized ultrasonic Doppler velocimetry (UDV). Two ultrasound transponders (8 MHz, 8 mm in diameter) were placed in the endwall at the heated end of the box such that their beams were horizontal, one centred 15 mm above the base and the other 30 mm below the lid (both on the spanwise centreline of the box), so as to measure the horizontal x component of velocity u in the bottom boundary layer and the top plume outflow. A third (4 MHz) transponder was placed in the lid, its beam directed vertically downward near the plume, centred 25 mm from the endwall (again on the centreline of the box), so as to measure the vertical component w of velocity. The technique required the suspension of 75–125 μm Pliolite particles throughout a prolonged period. Hence, the density of the working fluid in these runs was increased to 1021 kg m^3 using sodium chloride. Despite measures to achieve a very close match of densities, it was not possible to retain sufficient numbers of particles suitable for UDV (or particle image velocimetry) in suspension for 10–20 days throughout an initial equilibration period, a change of boundary conditions and the subsequent re-equilibration. Particles were therefore carefully injected into the box over about 1 hour, in 35 ml of water and surfactant at the same temperature as the tank, around 6 h before changing the boundary conditions. This allowed much of the adjustment to be monitored, but not the later stages of the re-equilibration, as small amounts of sedimentation of the particles onto the base led to a drift in the boundary heat flux and interior temperatures. Depending on the number density of particles, horizontal velocity was adequately determined in up to 223 gates along a beam up to 300 mm long, and vertical velocity was measured in 147 gates covering the full depth of the box. The beams expanded with distance to 20 mm wide at 200 mm from the probe, a width exceeding the boundary-layer thickness and plume width. The measurements gave an average of the along-beam velocity component over the beam width.

In separate runs dedicated to dye flow visualization a uniformly illuminated white screen was placed behind the box on the far side from cameras, and the insulation boards were removed from the two long sidewalls for viewing periods.

3.2. *Experimental parameters and method*

The governing parameters are the relevant Rayleigh number (2.1), along with the Prandtl number and two aspect ratios,

$$Pr \equiv \frac{\nu}{\kappa}, \quad A \equiv D/L, \quad B \equiv W/L. \tag{3.1}$$

The Rayleigh number is defined here in terms of the fluid properties (c_p, ν, κ and ρ_0) at the measured temperature of the heating portion of the copper boundary (table 2). This definition avoids ambiguity associated with variation of the physical properties of water with temperature: in the present experiments the thermal expansion coefficient is roughly three times larger at the hot boundary than at the cold boundary. We choose to define parameters in terms of the properties at the highest temperature because these determine the dynamically important destabilizing buoyancy flux (Hughes & Griffiths 2006; Hughes *et al.* 2007). In most experiments $Ra = 1.3 \times 10^{12}$ or $Ra_F = 1.8 \times 10^{14}$, $Pr = 5.2$ and $A = 0.16$ (conditions close to those for run 3 of Mullarney *et al.* (2004) except that water properties were there evaluated at the marginally cooler interior temperature). The two additional experiments with a larger power input (experiments

https://doi.org/10.1017/jfm.2013.244 Published online by Cambridge University Press

T_H (°C)	κ (m^2 s^{-1})	ν (m^2 s^{-1})	α (K^{-1})	ρ_0 (kg m^{-3})
33.9	1.47×10^{-7}	7.7×10^{-7}	3.36×10^{-4}	0.994
44.5	1.54×10^{-7}	6.2×10^{-7}	4.17×10^{-4}	0.990

TABLE 2. Indicative values of the physical properties of water at the nominal heating boundary temperatures T_H for two of the equilibrium conditions in the laboratory experiments (see the text for definitions). Values used in calculations are evaluated at the actual hot boundary temperature T_H relevant to each experiment. Specific heat is $c_p = 4178.3$ J kg^{-1} K^{-1}.

10, 11; table 1) had $Ra_F = 5.1 \times 10^{14}$ and $Pr = 4.0$. These Rayleigh numbers changed by approximately 12 % following the boundary perturbations.

Experiments began with equilibration of the box to the initial boundary conditions. Temperatures showed no long-term secular change after 2 or 3 days and the system was left in this equilibrium state in order to record the mean properties over a further 2 days. The boundary conditions were then modified by changing the temperature of one of the water baths or the power setting of the electrical heating, and the subsequent adjustment was logged. Given the diffusion time through the depth ($D^2/\kappa = 3.1$ days) several of the final equilibrium states were monitored for at least 10 days after the boundary perturbation. Periods of 2–4 days were used to evaluate mean quantities in the final state. Experiments were generally carried out in pairs: the first of each pair began with the 'standard' conditions (cold bath 10 °C and either hot bath 34 °C or input power 280 W), then destabilized by increasing either the cooling temperature or the heating; after the second equilibrium state had been examined, that state was used as the initial condition for the next experiment in which the previous boundary perturbation was reversed. This was repeated for changes to both heating and cooling regions. The methodology confirmed that the same equilibrium state was approached from the opposite direction.

The magnitude of boundary perturbations was chosen large enough to allow detailed resolution of the temperature changes, but small enough that the changes did not overwhelm the initial boundary layer stratification (in distinction from thermal equilibration from an initially homogeneous fluid). The bath temperature was changed by 4.0 °C (approximately 17 % of ΔT) or the power input was changed by 20.0 W (10 % of Q). The temperature in the water baths increased to the new settings within 2 min. The power to the heating mat changed instantly, but the heat flux into the tank is estimated to take approximately 1 min to reach its new value (as a result of the heat capacity of the copper base). The cold water bath took around 3 min to cool after the setting was changed from 14.0 to 10.0 °C, assisted by rapid addition of prechilled water to the bath. These boundary perturbations were two orders of magnitude greater than the internal temperature fluctuations (±0.04 °C) in the equilibrium states.

An additional series of experiments was designed to search for a threshold in the magnitude of boundary perturbation that causes a shut down of the plume convection and formation of a shallow convection cell: using applied temperatures, the heating temperature T_H was decreased by 0.5, 1, 2 and 4 °C (table 1), corresponding to boundary changes 2.4, 4.8, 9.5 and 19 % of ΔT_1.

In reporting the results we group the various cases into the two classes of boundary perturbation that led to a net warming of the box: increased heating (either by Q or T_H) and increased T_C. There are also two classes that led to a net cooling: decreased

https://doi.org/10.1017/jfm.2013.244 Published online by Cambridge University Press

heating or decreased T_C. Each of these four classes involves the subclasses of applied heat flux Q or applied temperature difference ΔT.

4. Experimental results

4.1. *Equilibrium states*

The convection reached equilibrium states (such as the first and last frames of figure 1) that were identical to those described in Mullarney *et al.* (2004), Coman, Griffiths & Hughes (2010) and Stewart *et al.* (2011). There was very little dependence on ambient room temperature, excepting that the equilibrium temperature outside the boundary layer was smaller by 0.7 °C ($0.03\Delta T$) when the room temperature was 5 °C cooler than the box, and the secondary intrusion immediately above the boundary layer was slightly more pronounced for matched room temperature. The equilibrated flow was unsteady, because instability above the heated portion of the base modified the lower part of the stratified boundary layer into a convective mixed layer. Eddies produced at the plume and internal waves generated from the mixed layer travelled together along the length of the box. Temperature fluctuations were up to around 0.04 °C ($2 \times 10^{-3}\Delta T$) and standard deviations in the time averages for individual thermistor records were between 0.004 and 0.02 °C. Quantities consistent with previous work include the numerical constants for boundary layer thickness $(h/L)Ra^{1/5} = 2.7 \pm 0.2$ and velocity $(u_{bl}L/\kappa)Ra^{-2/5} = 3.8 \pm 0.2$, where we again assume the Rossby (1965) scaling. The interior temperature (based on time averages from the thermistor at $z/D = 0.875$ and the measured temperatures in the heating and cooling parts of the copper base) is for applied temperature differences $\hat{T}_{top} = 0.92$ and for imposed heat flux $\hat{T}_{top} = 0.89$ (each with a systematic uncertainty ± 0.03 arising from absolute temperature calibrations of thermistors in the water and the copper base).

4.2. *Warming adjustments*

When an equilibrium state was perturbed by increasing the heat input (either by imposed heat flux or temperature), there was a rapid and large increase of velocities in all parts of the box (figure 1). The response was most obvious as more vigorous small-scale convection within the heated parts of the boundary layer, and a warmer, faster endwall plume. The changes were clear 30 s after the boundary condition was changed. Noting that the diffusion time through the cold boundary layer thickness was $h^2/\kappa \sim 700$ s, this response reflects rapid transfer of heat from the heating boundary by the small-scale convection. The faster flow out of the boundary layer and into the plume also caused a thinning (hence, warming at any given height) of the boundary layer above the cooling plate. The surge in the convection resulting from the flux imbalance was far out of proportion to the small change in Q or ΔT. However, the flow was not like that seen when thermal forcing is first applied to a box of initially uniform temperature (Mori & Niino 2002, see also the DNS in § 5): at the small amplitude of boundary condition change used here the pre-existing boundary layer stratification continued to confine the instability to a shallow convective layer, and vertical motion penetrated into the interior only near the endwall.

Temperature changes in the interior began with anomalously warm water being carried to the top of the box by the plume and flowing along the top as a gravity current. The current occupied the upper 25 % of the box depth and was initially driven by a greater horizontal buoyancy difference than that driving the plume outflow in the equilibrium states. After the stronger current reached the far endwall, a large-amplitude internal wave propagated along the box in the opposite direction on the existing

https://doi.org/10.1017/jfm.2013.244 Published online by Cambridge University Press

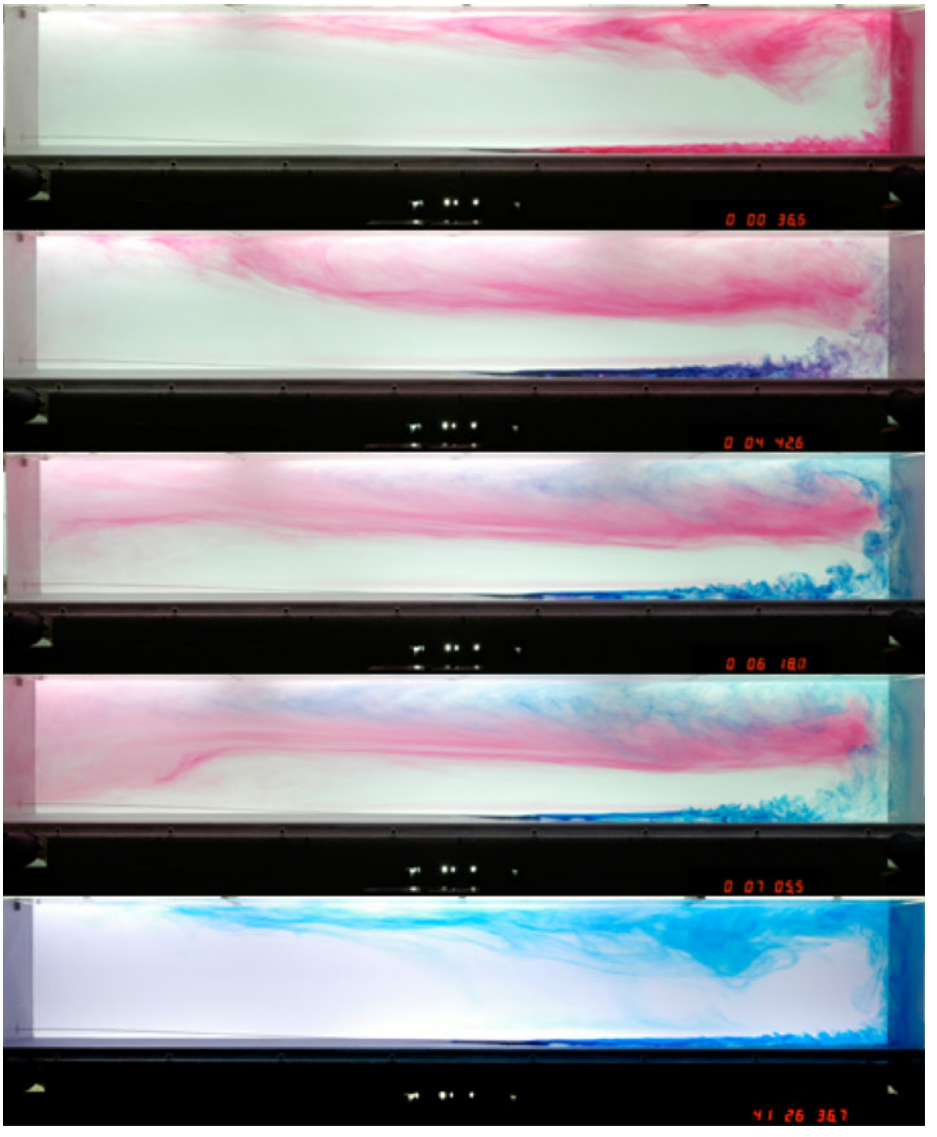


FIGURE 1. Photographs of passive dye marker in the flow for a case of an applied temperature difference and an increase of the heating temperature T_H from 34 to 38 °C (repeat of experiment 14, table 1, for the purpose of photography; see Movie 1 of the online supplementary material). Neutrally buoyant dye was slowly released into the bottom boundary layer near the midpoint of the box. It was carried to the right over the heated base, picked up by the small-scale convection and carried up in the endwall plume. The dye colour was changed from red to blue at the time the base temperature was increased (and the clock restarted from zero). Small-scale convection began to be more vigorous within 1 min, penetrating more of the overlying stable boundary layer and accelerating the plume, even before the blue dye had reached the plume. There was a surge of motion throughout the box. From top to bottom the times relative to the change of boundary condition time are: $t = 0$ (the initial equilibrium state); $t = 4.6$ min; $t = 6.3$ min; $t = 7.1$ min; and $t = 41$ h (a separate release of dye during the final equilibrium state). After around 30 min the flow velocities began to visibly reduce. There was no visible difference between the motions in the initial and final states.

https://doi.org/10.1017/jfm.2013.244 Published online by Cambridge University Press

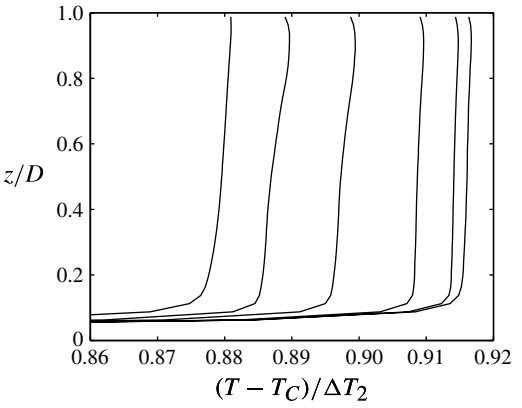


FIGURE 2. Vertical profiles of temperature after the applied heating temperature T_H was increased by 1 °C (experiment 18, table 1). Profiles are at the midpoint $x/L = 0.5$, $y/W = 0.5$ and normalized as $\hat{T} = (T - T_C)/\Delta T_2$, where $\Delta T_2 = T_{H2} - T_C$ is the applied boundary difference in the base *after* the perturbation. Thus, the initial equilibrium profile (on the left) is normalized by final conditions. The profiles warm monotonically in time toward the final equilibrated state (on the right). The boundary change was imposed at 3.3×10^5 s after startup, each profile shown is an average over 25 profiles taken at 2 min intervals, the averaging period ($\delta\hat{t}_D = 0.011$) starting at (3.0, 3.34, 3.38, 3.5, 3.86 and 5.8) $\times 10^5$ s (i.e. relative to the perturbation time $\hat{t}_D = -0.11$, 0.0147, 0.0294, 0.0735, 0.206 and 0.919). The plot is truncated at $\hat{T} = 0.86$ ($T \approx 29.6$ °C), hence it does not show most of the boundary layer, which at this location goes to the cold boundary temperature $\hat{T} = 0$ at $z = 0$.

stratification near mid-depth (fourth panel of figure 1). Features of the circulation revealed by tracer are a uniform downward displacement of water in the interior and substantial re-entrainment into the plume, which thinned the vertical extent of horizontal layers of tracer in the interior and left only a fraction of the plume outflow transport reaching the bottom boundary layer. An example of the adjustment of temperature and stratification for a small (1 °C) increase in T_H is shown in figure 2. A very short time (∼10 min) after the change the average temperature gradient in the interior had increased many times above the equilibrium value 0.4 °C m^{-1}, but after just ∼20 min the plume had flushed the box volume and the temperature proceeded to increase at all depths. After 1 h (second profile from the left) the gradient had decreased towards its initial value. Given the short time, this adjustment was achieved purely by advection in the interior.

UDV measurements (figure 3) showed that velocities increased rapidly, reaching a maximum around 20 min after the boundary perturbation, then slowly decreased toward the final equilibrium values. The velocity measurements shown, however, do not resolve the maximum as they represent time averages over 24 min and averages over the width of the ultrasound beams (20 mm wide at 200 mm distance from the transducers). The small increase in both $\hat{u}$ and $\hat{w}$ between the two equilibrium states is consistent with the 17 % change in ΔT and the established scaling law $\hat{u}, \hat{w} \sim Ra^{2/5}$, whereas the transient surge had a maximum in $\hat{u}$ (despite the averaging) greater than six times the velocities in either equilibrium state. The variations of the horizontal velocity in the plume outflow at different distances from the endwall (figure 3*a*) show that observations at any one location are not a good guide to the overall adjustment process, as each record includes the effects of unsteadiness in the meanders and

https://doi.org/10.1017/jfm.2013.244 Published online by Cambridge University Press

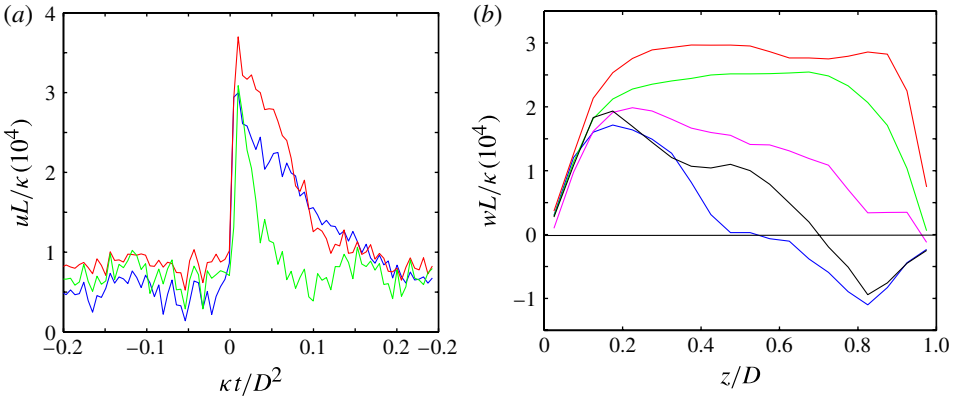


FIGURE 3. Velocity measurements after the heating temperature T_H was increased by 1 °C (experiment 17, table 1), corresponding to the temperature evolution in figure 2. The boundary change was imposed at 0.7×10^5 s after start up. (*a*) Horizontal velocity $\hat{u}$ in the plume outflow at three positions from the endwall, from the horizontal ultrasound beam centred at $z/D = 0.85$: records shown are at $x = 55$ mm (blue), 105 mm (red) and 155 mm (green). (*b*) Vertical profiles of vertical velocity $\hat{w}$ near the plume as a function of time after the change of boundary temperature, from the vertical ultrasound beam centred at $x = 20$ mm: profiles are at times, relative to the perturbation time $t = 0$, $\hat{t}_D = -0.088$ (blue, initial equilibrium), 0.0221 (red), 0.0588 (green), 0.132 (magenta) and 0.235 (black, final equilibrium). All results shown are averages over 12 profiles (each profile based on 900 pulses) taken over approximately 24 min. The time averaging and beam width both cause substantial reduction of the velocity maximum in (*a*). Note that time is scaled by D^2/κ, velocity by κ/L.

formation of eddies. Profiles of vertical velocity, measured near the outer edge of the plume (figure 3*b*), showed a maximum in the lower part of the box (near $z/D = 0.2$) in the initial and final states, and downward flow in the upper parts of the box (as a result of a downward flow outside the plume; see DNS solutions in § 5.2). During the surge the plume created a stronger and wider upflow at all depths in the profile, and the surge persisted for approximately $\hat{t}_D \approx 0.1$ (3×10^4 s; upper three profiles). Again the time-averaging limits the resolution of the maximum in $\hat{w}$. Note also that given the increase in width of the upflow, the velocity increase alone does not indicate the magnitude of the surge in transport.

Similar behaviour was observed in cases where the cooling temperature T_C at the other end of the base was increased. This class of perturbation again led to a net buoyancy input and net warming of the box. There was a very small additional delay (of 2–4 min) in the onset of the surge, as the increased boundary temperature can be communicated within the stably stratified boundary layer only by conduction, and additional time is also required for the reduced boundary-layer stability to be carried horizontally to the heated end, where the small-scale convection then became more vigorous. Video records reveal a weaker velocity surge after an increase in the cooling temperature compared to that for an increase of the heating temperature. However, there was no other apparent distinction between these two classes of boundary perturbation.

Temperatures at all locations monotonically increased from that in the initial state, T_1, to that in the final state, T_2. These states were defined by the time-averaged temperatures evaluated over at least 2 days with no secular change. The adjustment is shown by the deviation from the final state, $\Theta(t) \equiv (T - T_2)/(T_1 - T_2)$, examples

https://doi.org/10.1017/jfm.2013.244 Published online by Cambridge University Press

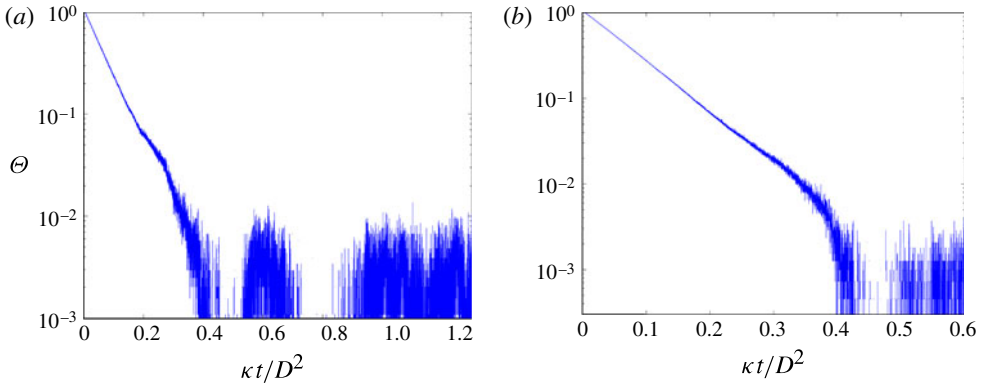


FIGURE 4. (Colour online) Examples of temperature evolution in net warming cases, as measured in the interior of the box ($z = 0.875$ above centre of cooling region) for the cases of (*a*) fixed heating flux and an increase of the applied heating power Q with fixed cooling temperature (experiment 10, table 1) and (*b*) an increase in the cooling boundary temperature T_C (experiment 7). Boundary perturbations were applied at $t = 0$. The normalized temperature deviation Θ (equation (2.9)) oscillates about zero at $\hat{t}_D > 0.4$ (only positive values are plotted). The individual thermistor records shown give e-folding times $\kappa\tau_e/D^2 = 0.073$ and 0.074 for the two different boundary perturbations (straight lines having these slopes accurately overlay the data through more than 90 % of the final temperature adjustment), and the respective averages over all eight fixed thermistor locations are 0.073 ± 0.002 and 0.074 ± 0.001. The apparently sharper decrease in Θ and deviation from an exponential near $\hat{t}_D = 0.4$ can be attributed to variability in the flow at large time and uncertainties of 0.004/0.008 °C in the final equilibrium temperature T_2.

of which are shown in figure 4 for an increase in either the heat input Q or the cooling temperature T_C. After the first 30 min of the adjustment, the further evolution was the same at all locations, including in the thermal boundary layer. In all warming adjustments the evolution was well described by an exponential of the form (2.9) or (2.18), through 95 % of the change in most runs and through over 99 % for the examples shown in figure 4. At large times the difference $T - T_2$ became dominated by the fluctuations in the flow, and eventually fluctuated in sign. The overall behaviour was similar for all four classes of warming perturbation, independent of whether the increase was at the heating or cooling region, or with imposed flux or temperature. The measured time scales will be discussed in § 6.

4.3. *Cooling adjustments*

The equilibrium states reached at the end of the warming experiments were subsequently perturbed by reversing the previous change of boundary conditions: the heating power Q or the heating temperature T_H were decreased to their original values (to within ±0.05 W or ±0.01 °C). This forced a net cooling of the box. As illustrated in figures 5 and 6, the flow evolved in a very different manner: the plume upwelling suddenly ceased (within approximately 1 min) and water exiting the boundary layer in the plume began to return in a horizontal intrusion immediately above the boundary layer. The change generated a large-amplitude solitary wave of elevation on the density stratification that propagated the length of the box ahead of the intrusion. The small-scale convection over the heated base weakened and penetrated less into the overlying stable boundary layer. A closed shallow circulation cell formed over the length of the

https://doi.org/10.1017/jfm.2013.244 Published online by Cambridge University Press

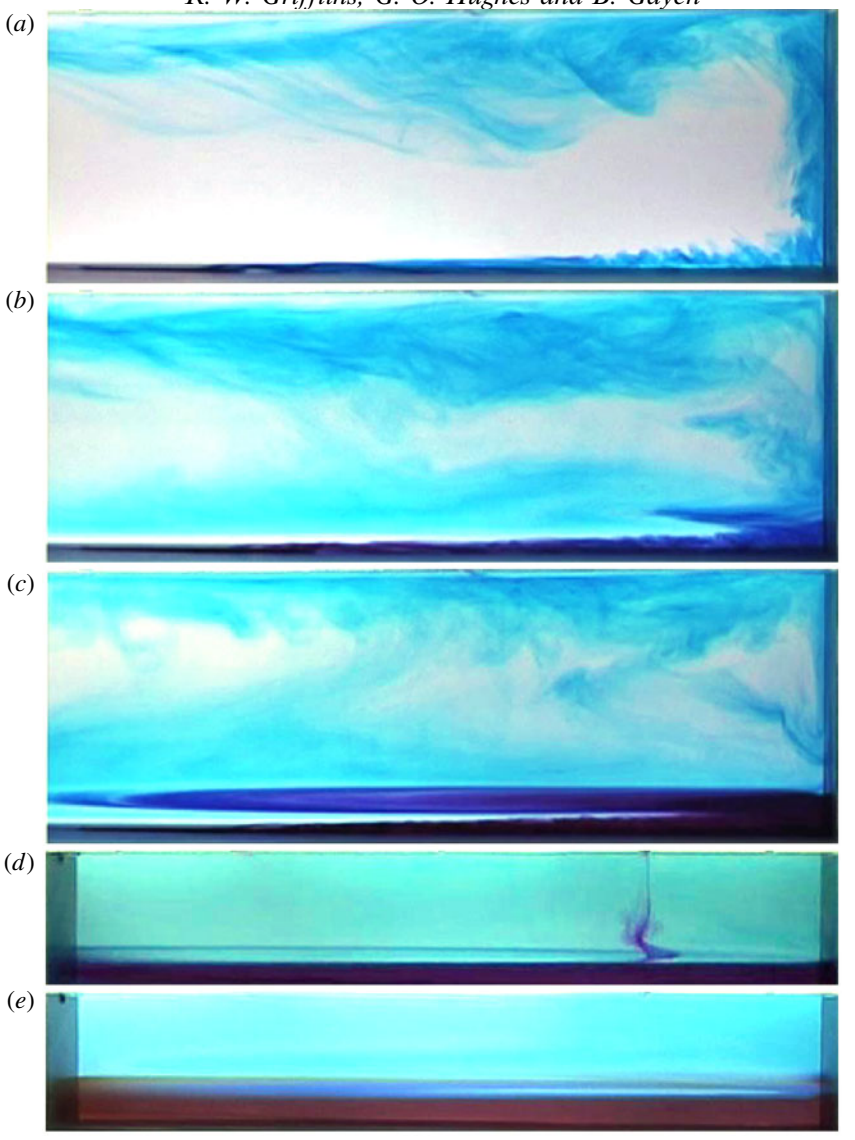


FIGURE 5. (Colour online) Evolution of convection after a decrease of the applied heating flux (repeat of experiment 6, table 1 for visualization; see Movie 2 of the online supplementary material). Blue dye tracer is initially released slowly at the midpoint of the base, and at 30 min (fourth frame) $KMnO_4$ crystals are dropped from the top and sit on the base until dissolved. The convection was first equilibrated to the initial conditions for 41 h 34 min but times given are elapsed time after the boundary perturbation was imposed. From top to bottom times after the perturbation are: (*a*) $t = 0$ (the initial equilibrium state); (*b*) $t = 2$ min 19 s; (*c*) $t = 8$ min; (*d*) $t = 31$ min; (*e*) $t = 6$ h 34 min. The first three images show the heated half of the box length, the bottom two show the whole box. The endwall plume suddenly stopped at $t = 50$–60 s and a horizontal intrusion began (at $t = 1.0$ min, second frame), forming a cold circulation cell capped above, at $t \sim 10$ min, by an interface at $z = 30$ mm; no motion could be seen in the overlying interior; by $t \sim 31$ min there was a second shallow cell (the first circulation cell is dark with dye and ~40 mm deep). In this run the plume reached the top by $t \sim 15$ h but the lateral plume outflow remained at a shallower level until after 26 h, and full-depth overturning was fully re-established by 47 h. There was no visible difference between the motion in initial and final states.

https://doi.org/10.1017/jfm.2013.244 Published online by Cambridge University Press

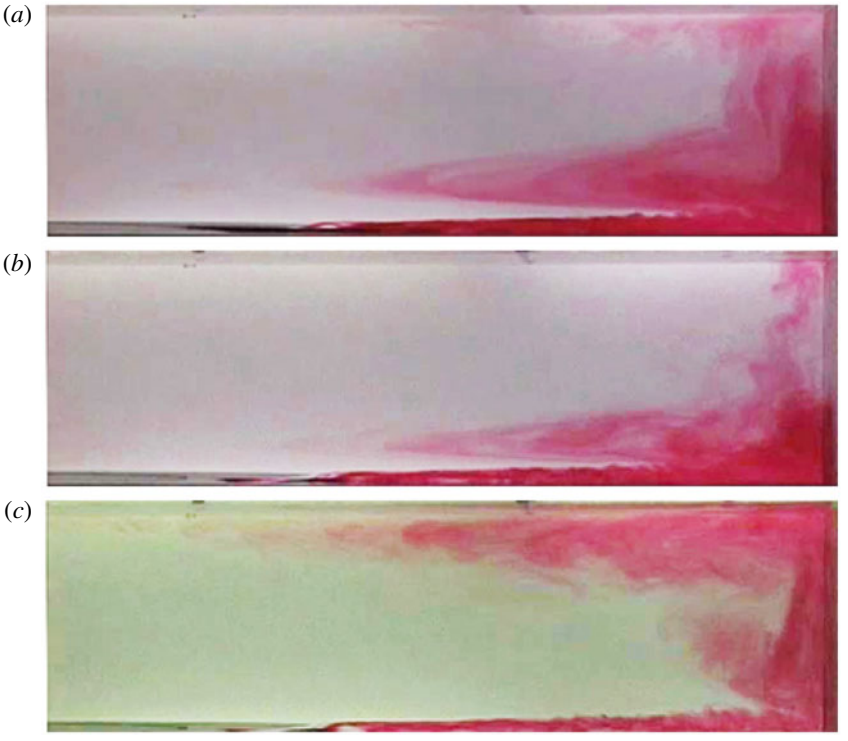


FIGURE 6. (Colour online) Photographs after the cooling temperature T_C was decreased for a fixed heating temperature T_H (repeat of experiment 9, table 1 for photography; see Movie 3 of the online supplementary material). Times after the boundary perturbation was imposed, from top to bottom: (*a*) $t = 13$ min; (*b*) $t = 59$ min; (*c*) $t = 9$ h 12 min. Separate dye releases were made ∼5 min before each image. Images show 3/4 of the box length. The plume was unaffected until $t = 5$ min, after which it quickly weakened; a horizontal intrusion started at $t = 6$ min; the plume continued to reach the top of the box until $t = 9$ min, and the intrusion length marked by dye at that time was roughly equal to the depth of the box, with its upper edge at 80 mm above the bottom; a shallow circulation cell was clearly outlined by $t \sim 20$ min but the endwall plume continued to penetrate much of the depth of the box in an unsteady, fountain-like behaviour, the water falling back to join the horizontal flow in the upper part of the shallow cell; the greatest stabilization of the overturning appeared to be at around 30 min; the plume thereafter became increasingly unsteady, with large-amplitude oscillations and eddies reaching the top of the box at $t = 1$ h; the plume permanently reached the top after 4.5 h but all of the transport fell back into the shallow cell, until at 5 h an intrusion began to flow intermittently along the top boundary; and at $t = 9$ h all of the transport switched to a plume outflow along the top; a very weak intrusion persisted at 80 mm from the bottom for several hours; and the convection returned to the equilibrium full-depth overturning at around 15 h.

box, occupying 20–25 % of the box depth. After around 10 min the shallow intrusion had carried dye from the boundary layer to the far end of the box (figure 5*c*). Above the shallow recirculation there appeared to be no significant motion. A second, weaker and shallower circulation cell formed above the first at around 20 min, the direction of motion consistent with transfer of momentum upward from the lower cell by interfacial stress. This second cell persisted for 6–7 h, with no visible circulation in the overlying region.

https://doi.org/10.1017/jfm.2013.244 Published online by Cambridge University Press

In the case of decreased applied heating temperature (figure 5), one shallow cell was left after 8 h, filling approximately one third the depth of the box. By this time the endwall plume had become more active within the lower cell and buoyant eddies had also begun to penetrate a small distance into the stagnant water above the cell. The height of this penetrative convection subsequently increased, with large oscillations, the top of the plume fluctuating between the interface height and the top of the box. At $t \sim 10$ h the plume penetrated permanently to the top of the box, but also formed a downward flow beside the plume, with the outflow remaining below mid-depth. Thereafter the outflow slowly migrated upward until, at $t \geqslant 26$ h, the convection had returned to its original pattern with a horizontal outflow along the top and a single-cell overturning of the whole box. Overall, the evolution was qualitatively similar to that previously reported in experiments initiated with a homogeneous box at a temperature greater than T_H (Mullarney *et al.* 2004).

When the cooling temperature T_C was decreased (figure 6), the increased stability of the bottom boundary layer developed above the cooling boundary was carried to the heating boundary, where it tended to reduce convective instability and the thickness of the convective mixed layer. The endwall plume was again quickly suppressed and a horizontal return flow formed immediately above the boundary layer. Compared with the case with a decrease in T_H, this change took longer (6 min), the shallow cell was up to twice as deep, the plume appeared more active at all times and the evolution at larger times did not involve substantial deepening of the shallow cell. Instead, the plume penetrated higher and higher as an intermittent, oscillatory fountain, and reached the top at 4.5 h (while its outflow continued to fall back into the lower cell). After 9 h the plume suddenly switched, thereafter feeding an outflow along the top boundary.

The two cooling classes above showed similar temperature and velocity evolution. Unlike in the warming cases, temperature adjustment in the interior was a function of height, as illustrated by the vertical profiles in figure 7. The initial response was a relatively rapid decrease of temperature in, and at depths a little above, the boundary layer, where the shallow circulation cell formed. Once the shallow circulation cell approached an approximate heat balance with the bottom boundary conditions its temperature proceeded to decrease much more slowly. In the overlying stagnant region the temperatures decreased very slowly and steadily throughout the adjustment. Vertical velocities in the plume vanished immediately after the boundary perturbation and recovered very slowly during the stably stratified period. However, velocity measurements in this case were compromised by evolution times that were long compared with the particle sedimentation times.

The overall cooling evolution took longer than in the warming cases. Plots of Θ at various heights (figure 8) shows that trends were far from exponential. In particular, the lower parts of the water column cooled relatively rapidly at small times after the boundary perturbation, whereas the upper parts did not begin to respond significantly until long after the shallow circulation cell had cooled, hence the larger stratification seen in figure 7. The time scales will be discussed in § 6.

No threshold was found in the amplitude of stabilizing boundary perturbation that produced a shallow circulation cell. The boundary perturbations ($0.5° \leqslant \delta T \leqslant 4$ °C) corresponded to $0.024 \leqslant \delta T/\Delta T \leqslant 0.19$. Even the smallest of these values led to a temporary collapse of the endwall plume, a return of boundary layer water in an intrusion immediately above the boundary layer, and confinement of all significant flow to a shallow cell. Our starting hypothesis was that the initial equilibrium interior temperature $\hat{T} = 0.92 \pm 0.02$ (for imposed ΔT) measured in the laboratory flows

https://doi.org/10.1017/jfm.2013.244 Published online by Cambridge University Press

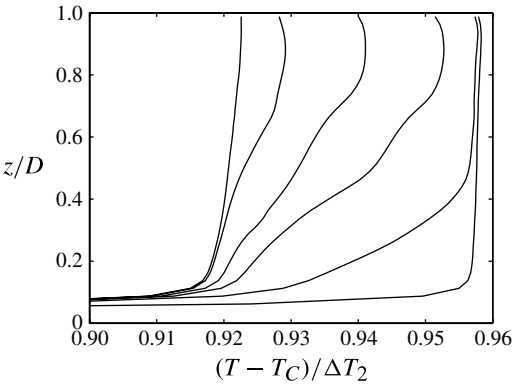


FIGURE 7. Vertical profiles of temperature during a cooling adjustment following a reduction of the heating temperature T_H by 1 °C, for applied temperature boundary conditions (experiment 19, table 1). This reversed the boundary perturbation of figure 2. Temperature is normalized as $\hat{T} = (T - T_C)/\Delta T_2$, where ΔT_2 is the boundary temperature difference *after* the perturbation, and temperature changes monotonically from the initial equilibrium state on the right to the final equilibrium state on the left. Profiles are at the midpoint $x/L = 0.5$ and each is an average of 25 profiles at intervals of 2 min. In dimensionless terms the starting times (relative to the perturbation time) are $\hat{t}_D = -0.018$ (initial equilibrium), 0.0919, 0.165, 0.276, 0.459 and 0.974 (final equilibrium). Plot is truncated at $\hat{T} = 0.9$ ($T \approx 29.6$ °C) and temperatures go to $\hat{T} = 0$ at $z = 0$.

suggests that a reduction in heating boundary temperature approaching 10 % of ΔT may be required for the plume to be shut down. However, this hypothesis neglects the role of mixing and diffusion, which rapidly reduce the temperature excess in the plume (with height), leaving a plume temperature anomaly relative to the interior less than 1 % of ΔT. Thus, any threshold (if there is one) is too small to be resolved in the current experiments.

5. Direct numerical simulations

5.1. *Method*

Three-dimensional DNS were used to obtain solutions under conditions similar to those in the experiments, taking a channel of the same aspect ratio and a comparable Rayleigh number, forced by uniform temperatures T_H and T_C applied over each half of the base (figure 9). We assume a linear and Boussinesq fluid, and solve the dimensionless continuity, momentum and temperature equations:

$$\nabla \cdot \hat{\boldsymbol{u}} = 0, \quad \frac{\mathrm{D}\hat{\boldsymbol{u}}}{\mathrm{D}\hat{t}} = -\nabla \hat{p} + Pr\nabla^2 \hat{\boldsymbol{u}} + RaPr\hat{T}\boldsymbol{k}, \quad \frac{\mathrm{D}\hat{T}}{\mathrm{D}\hat{t}} = \nabla^2 \hat{T}, \tag{5.1}$$

where the dimensionless quantities (denoted by a hat as before) are the velocity $\hat{\boldsymbol{u}} = (\hat{u}, \hat{v}, \hat{w})$, the temperature $\hat{T}$ relative to the reference value (T_C), the deviation $\hat{p}$ from the background hydrostatic pressure and time $\hat{t}$. Scales for mass, length, time and temperature difference are $\rho_0 L^3$, L, L^2/κ and ΔT (or $T_h|_{max} - T_c$ for applied flux), respectively, and given the small aspect ratio we will again present results in terms of the renormalized time $\hat{t}_D = (L/D)^2\hat{t} = \kappa t/D^2$. The governing parameters are the Rayleigh number (2.1), Prandtl number and aspect ratios (3.1). The simulations were

https://doi.org/10.1017/jfm.2013.244 Published online by Cambridge University Press

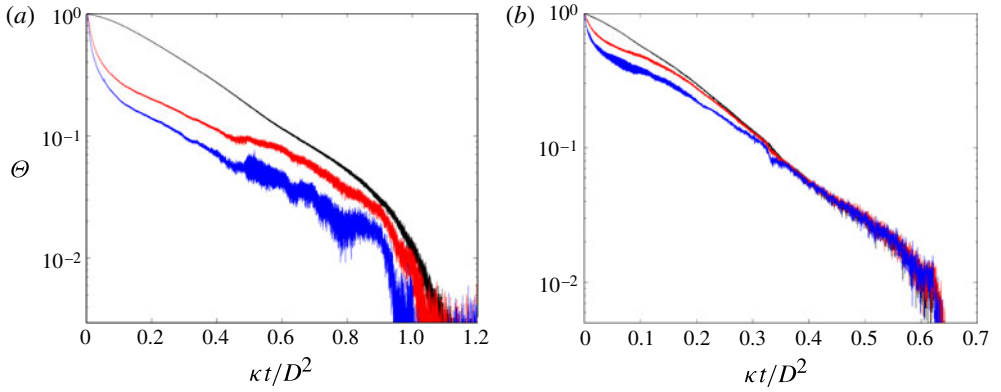


FIGURE 8. Evolution of temperatures at $z/D = 0.875$ (black), 0.5 (red) and 0.1 (blue) after (*a*) decreasing the cooling temperature T_C with a fixed heating flux (experiment 9 table 1, in which the boundary perturbation of figure 4*a* was reversed) and (*b*) decreasing the heating flux with fixed T_C (experiment 11, reversing the perturbation of figure 4*b*). Perturbations to the initial equilibrium, $\Theta = 1$, were made at $t = 0$. The highest measurement location was above the centre of the cooling region and in the deep stagnant layer; the mid-depth location was above the heating region; the lowest location was outside the boundary layer but within the shallow circulation cell that formed immediately after the boundary perturbation; the two lower sensors show more variability from small-scale convection and unsteadiness in the plume. The apparently faster decrease in (*a*) around $\hat{t}_D > 0.9$ ($t > 2.3 \times 10^5$ s) can be attributed to an uncertainty of order 0.005 °C in the final equilibrium temperature or to the large time fluctuations. Signals oscillated around $\Theta = 0$ at $\hat{t}_D > 1.1$ and 0.65, and only positive values are plotted.

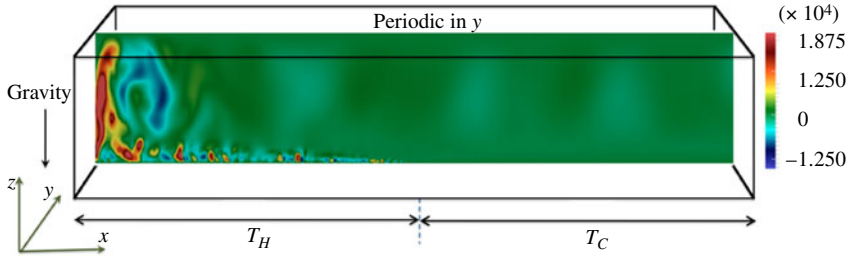


FIGURE 9. Schematic of the domain used for DNS: the hot plate temperature is T_H ($\hat{T} = 1$) on the left half of the base ($0 \leqslant \hat{x} < 1/2$) and the cold plate temperature is T_C ($\hat{T} = 0$) on the right half of the base ($1/2 < \hat{x} \leqslant 1$). Superposed is a snapshot of the dimensionless vertical velocity field $\hat{w}$ in the $\hat{x}$–$\hat{z}$ plane from the first thermally equilibrated numerical simulation. The colour scale shows velocity relative to the scale L^2/κ.

carried out for $Ra = (5.86,\ 6.63) \times 10^{11}$, $Pr = 5$ and $A = 0.16$ (corresponding to the laboratory tank with $\Delta T = 30$ °C and $\alpha = 2 \times 10^{-4}$ K^{-1}). The temperature-dependence of fluid properties was neglected in order to more clearly interpret the DNS results. Previous two-dimensional solutions for horizontal convection found no significant differences between the cases of constant fluid properties or the realistic temperature-dependent thermal expansion coefficient (Mullarney *et al.* 2004). All boundaries other

https://doi.org/10.1017/jfm.2013.244 Published online by Cambridge University Press

than the base were insulating. No-slip velocity conditions were applied on the top, bottom and endwalls.

The simulations used a mixed spectral/finite difference algorithm. The computational grid had $513 \times 128 \times 257$ points in the $\hat{x}$, $\hat{y}$ and $\hat{z}$ directions, respectively, with grid cells clustered toward the boundary layer and plume. As in previous two-dimensional solutions (Mullarney *et al.* 2004), it was particularly important to have sufficient grid resolution in the corner region, where the boundary layer becomes the plume. The box width was $W = 0.05L$ and velocity components were decomposed into spatial mean and turbulent quantities, defined as the spanwise ($\hat{y}$) average and variation. Periodicity was imposed in the $\hat{y}$ direction and derivatives were evaluated with a pseudo-spectral method. The grid was staggered in the vertical and streamwise directions and the corresponding derivatives computed with second-order finite differences. A low-storage third-order Runge–Kutta–Wray method was used for time stepping, except for the viscous terms, which were treated implicitly with the alternating direction implicit method. Variable time steps (of $O(10^{-8})$) were used such that the Courant–Friedrichs–Lewy number was unity. The grid resolution $\Delta_{x,y,z}$ was compared with the Batchelor microscale, $\eta_b \sim (Pr)^{-1/2}(\nu^3/\varepsilon)^{1/4}$ (where ϵ is the viscous dissipation rate) and satisfied the criteria $[\Delta_x, \Delta_y, \Delta_z]_{max}/\eta_b \leqslant \pi$ (proposed by Stevens, Verzicco & Lohse 2010) at all stages of the flow adjustment, including the relatively energetic early stages. A further strong test of adequate resolution is the result that the energy budget closed exactly with each term in the budget computed independently (Gayen *et al.* 2013).

The simulation was initialized with isothermal ($\hat{T} = 0.83$) and motionless fluid, but a small amount of white noise concentrated near the bottom boundary was added to the initial velocity field. Thermal forcing was applied and the temporal evolution of the solution (DNSa in table 1) was monitored using time series of temperature, the net heat input through the base, flow velocities, and mechanical energy conversion rates. After the first equilibrium state was approached (figure 10), integration was continued for a substantial time in order to test for slow secular change. Later, at $\hat{t}_D = 0.25$ ($\hat{t} = 6.4 \times 10^{-3}$ and corresponding to 12 h on the experiments), the base heating temperature was increased from $\hat{T}_H = 1$ to $\hat{T}_H = 1.133$ (corresponding to a change $\Delta T = 30$ °C to $\Delta T = 34$ °C under the laboratory conditions) and the solution (DNSb) allowed to reach a second equilibrium state (at $Ra = 6.63 \times 10^{11}$). Finally, T_H was reduced back to the previous value and the equilibration (DNSc) run to 99 % completion (beyond this the slow cooling became too expensive in CPU time). In a separate simulation the temperature boundary condition at the heating end was replaced by a uniform heat flux equal to the average heating flux in the applied temperature case, giving $Ra_F = 6.41 \times 10^{13}$ (DNSd in table 1).

5.2. *DNS results*

Temperatures at three locations in the flow are plotted in figure 10, which shows the responses to the three boundary perturbations. The thermally equilibrated states were identified as having no secular variation in any quantity. However, equilibrium states are characterized by significant fluctuations about mean values, such as the horizontal average temperature $\hat{T}_{top}$ (±0.2 %), the net basal heat input (±2 % of the heat throughput, see below) and the total rate of production of kinetic energy (±5 %) (Gayen *et al.* 2013). The persistent fluctuations were associated with eddies that form at the plume end and travel slowly along the length of the box in the interior region, one set of eddies travelling just above the bottom boundary layer and another near the

https://doi.org/10.1017/jfm.2013.244 Published online by Cambridge University Press

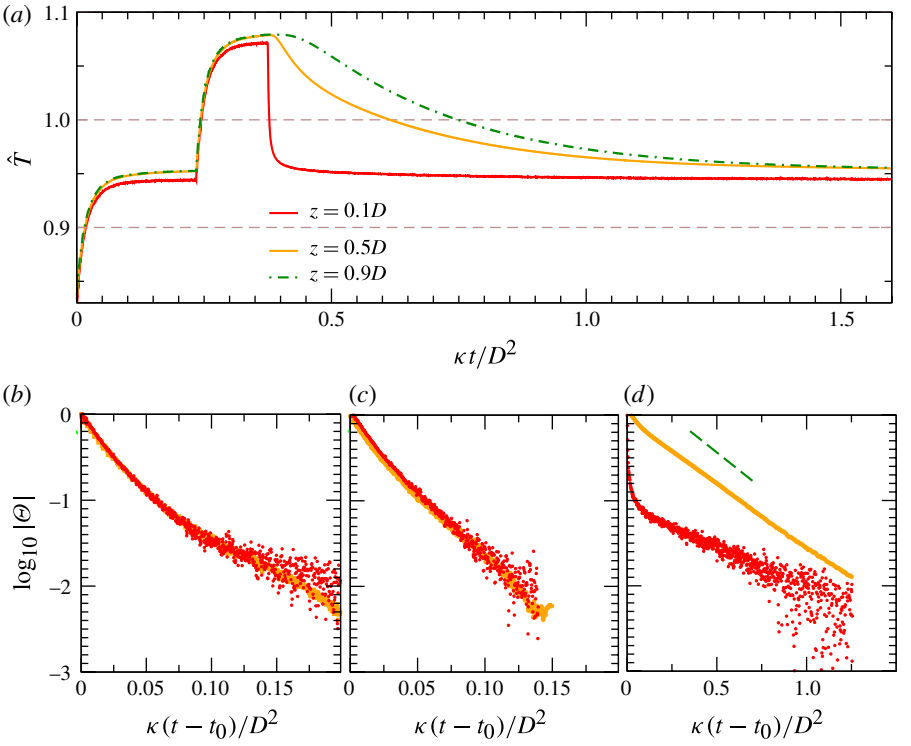


FIGURE 10. (Colour online) The evolution of temperature given by DNS. (*a*) Horizontal averages (excluding the plume) of $\hat{T} = (T(z,t) - T_C)/\Delta T$ at three heights $z/D = 0.1$ (dark grey, shown in red online), 0.5 (light grey, shown in orange online) and 0.9 (broken line). Imposed temperatures were $\hat{T}_H = 1$ and $\hat{T}_C = 0$, the fluid was initially homogeneous at $\hat{T} = 0.83$ and the interior equilibrated to $\hat{T} = 0.952$. The heating temperature was later increased to $\hat{T}_H = 1.133$ in order to perturb the existing convective state, and finally decreased back to its initial value. (*b–d*) Normalized deviations Θ from the relevant equilibrium value T_2, at $z/D = 0.1$ and 0.5, with the time origin for each of the three adjustments set to the time $\kappa t_0/D^2 \approx 0, 0.25, 0.38$ of the boundary changes. The sign of Θ fluctuates in the late stages of equilibration: the absolute value is plotted here. The short broken line in (*d*) shows the slope of the conduction solution (2.22) with stagnant layer depth $d = 0.8D$, which approximately matches the temperature adjustment of the upper region in the DNS.

top of the box. These eddies are closely linked to an internal wave mode, which is recognized by sloping phase lines that reflect between the upper and lower boundaries. Equilibrium temperatures T_1 and T_2 at the desired locations are again defined as time averages in the relevant equilibrium state.

The solution approached the first two equilibrium states (figure 10*b,c*) in a simple exponential manner, the temperatures everywhere reaching the final time-averaged values to within $\Theta < 10^{-2}$ (and $T_2 - T < 1.3 \times 10^{-3}\Delta T$) at $\hat{t}_D \approx 0.16$. The corresponding result for the net boundary heat flux (figure 11), measured relative to the heat throughput and defined as

$$\left| \int_0^L \int_0^W \frac{\partial T}{\partial z} \, \mathrm{d}y \, \mathrm{d}x \right| \Big/ \int_0^L \int_0^W \frac{1}{2} \left| \frac{\partial T}{\partial z} \right| \mathrm{d}y \, \mathrm{d}x \leqslant 0.01 \quad \text{at } z = 0, \tag{5.2}$$

https://doi.org/10.1017/jfm.2013.244 Published online by Cambridge University Press

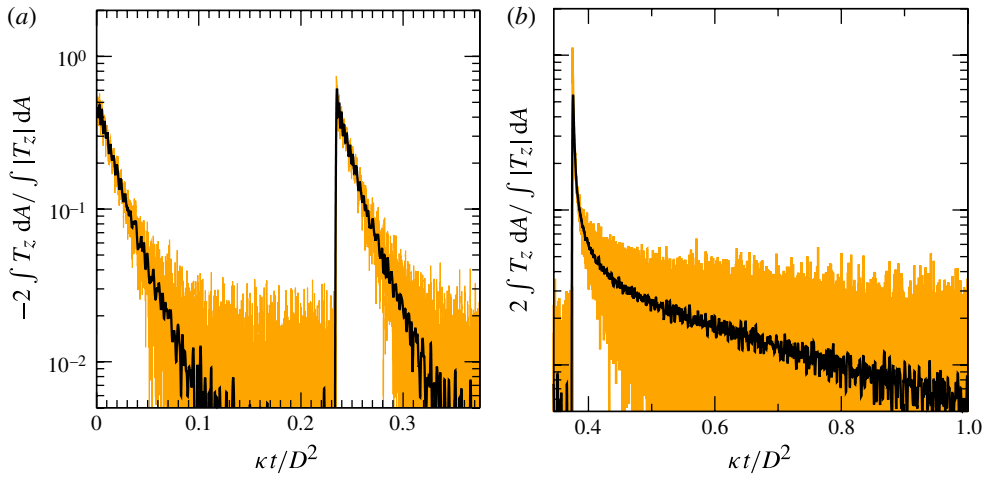


FIGURE 11. (Colour online) Time dependence of the net heat flux through the bottom boundary in the computed solutions, expressed as a fraction of the gross heat transport: (*a*) the two warming adjustments; (*b*) the cooling adjustment. The solution in light shade is averaged over intervals of 0.5 s (5 time steps) and the black line is a running mean in a moving window of 100 s. The initial 5 s after each boundary perturbation is omitted (net heat input is very large immediately after the perturbations). Only the positive values are plotted. As equilibrium states are approached ($\hat{t}_D > 0.15$ after a boundary perturbation) the flux imbalance fluctuates by $\pm 3\,\%$ about zero. Exponential fits to the two warming adjustments give the e-folding time scale $\kappa\tau_\Delta/D^2 = 0.022 \pm 0.001$. For the cooling adjustment in (*b*) two exponential regimes at early and late times give $\kappa\tau/D^2 = 0.0056 \pm 0.0003$ and $\kappa\tau/D^2 = 0.313 \pm 0.01$.

shows a similar exponential approach to equilibrium, and it then vanishes in an appropriate time average.

Snapshots of the velocity field are shown in figure 12 for the second adjustment of figure 10, following the warming boundary perturbation. Comparison of this case with the solution during the initial warming showed that the pre-existing density stratification of horizontal convection continues to confine the enhanced convection after the perturbation, whereas the homogeneous initial condition gave greater freedom for vertical motion in the early stages of convection. Otherwise, after a short time, the two flows are similar. For the case shown, peak vertical and horizontal velocities are five and eight times larger than those in the initial and final equilibrium states, consistent with values in the laboratory experiments (figure 3) after taking into account the time averaging used for the experimental data.

Mechanical energy conversion rates (Hughes *et al.* 2009; Gayen *et al.* 2013) were integrated over the volume of the box and are plotted in figure 14 after normalizing by $\Phi_i = -g\kappa WL(\langle\rho_D\rangle - \langle\rho_0\rangle)|_{equil}$ (where $\langle\cdot\rangle$ denotes a horizontal average and Φ_i is the conversion rate from internal to background potential energy by molecular diffusion down the mean gradient evaluated in the final equilibrium state). The equilibrium solutions (Gayen *et al.* 2013) have $\epsilon = \bar{\epsilon} + \epsilon' = \Phi_i$ and satisfy the required balance between the time-averaged buoyancy production of kinetic energy and viscous dissipation. The total production of turbulence by shear (Φ_T) is small in the equilibrium states, whereas the turbulent buoyancy flux (Φ_z' in figure 14) and turbulent dissipation rate (ϵ') are comparable to the corresponding mean flow quantities, and are in balance.

https://doi.org/10.1017/jfm.2013.244 Published online by Cambridge University Press

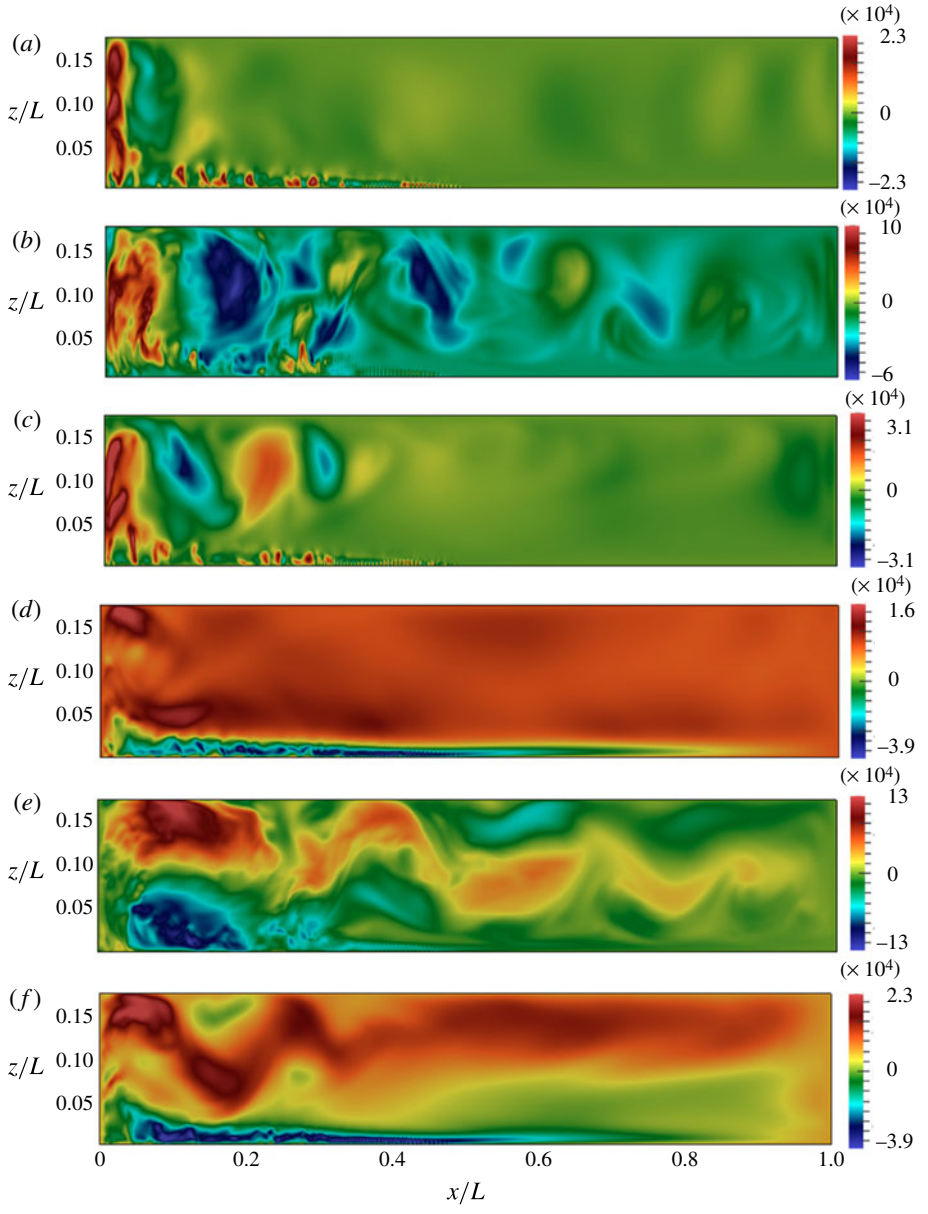


FIGURE 12. Snapshots of velocity components from the computed solution after the warming boundary perturbation in which T_H is increased (DNSb in table 1): (*a–c*) vertical velocity $\hat{w}$; (*d–f*) horizontal velocity $\hat{u}$; (*a,d*) from the initial equilibrium state; (*b,e*) at $\hat{t}_D = 1.55 \times 10^{-3}$ after the perturbation; (*c,f*) at $\hat{t}_D = 0.0796$. Velocities are scaled by κ/L. The colour scales are shifted as the flow evolves. See also Movie 4 of the online supplementary material.

In contrast to the equilibrium state, the flow after a warming boundary perturbation is characterized by production of turbulent kinetic energy at comparable rates from both mean shear and buoyancy fluxes. For the amplitude of perturbation applied here,

https://doi.org/10.1017/jfm.2013.244 Published online by Cambridge University Press

the buoyancy generation and dissipation rates pass through maxima around 10 times larger, and shear production of turbulence some 50 times larger, than those in the equilibrium states. Gayen *et al.* (2013) show that for a more complete understanding of the energetics of the equilibrium state it is necessary to look beyond the box-integrated quantities: conversions between available potential energy and kinetic energy in different regions of the flow dominate the energy budget by several orders of magnitude over the box-integrated values at these Rayleigh numbers. A conversion of available potential to kinetic energy in the plume is balanced by a similarly large reverse rate of conversion of kinetic to available potential energy in the interior region of the box. This conclusion carries over in a qualitative sense to the transient unbalanced convection, where the plume is much stronger than in the equilibrated flow. However, the volume integrated conversions in transient flows are sufficient for our purposes here.

A solution having imposed input heat flux and perturbed by increasing the heat input from Q_1 to Q_2 (DNSd in table 1), showed behaviour broadly similar to the warming with applied temperatures. The temperature changes were again closely described by an exponential. However, the adjustment was relatively slow.

For the stabilizing boundary perturbation the DNS again gives temperature evolution (figure 10*d*) consistent with the experiments. It also provides a check on the role of sidewall heat loss in the experiments during a long diffusive equilibration period. Snapshots of the velocity during the cooling adjustment are shown in figure 13. The reduction of T_H caused an immediate shutdown of the plume and the formation of a shallow circulation cell (figure 13*b,e*), which cooled rapidly until the net rate of boundary heat loss was comparable with the rate of heat gain into the shallow cell from the overlying, nearly stagnant water. Thereafter the shallow cell and the overlying stagnant region proceeded to cool slowly. The interior cooling is accompanied by a slow increase in plume penetration height (figure 13*c,f*) and a small increase in height of the bottom circulation cell. The cooling in the stagnant region can be compared to that expected by conduction alone: this region is approximately 70 % of the depth of the box during most of the adjustment, whereas the rate of cooling is the same as would be given by conduction through 80 % of the depth (shown by the broken line in figure 10*d*). Thus, conductive cooling through most of the depth is the dominant mechanism for thermal equilibration.

The mechanical energy budget reveals simply a rapid decrease in activity and a slow recovery towards the final equilibrium. Throughout the evolution the only significant conversions (in a box-integrated view) are production of mean flow by the release of available potential energy (supplied by surface buoyancy forcing), matched by viscous dissipation. The fluctuations are produced by convection, not by shear. The buoyancy fluxes and dissipation rates in the transient flow remain comparable for each of the mean and fluctuating components, as in the equilibrium states.

6. Adjustment time scales

In defining adjustment time scales we keep in mind that there may be more than one time scale of response for any given case, and also that time scales much longer than the duration of an experiment or solution are not resolved. On the other hand, in approaching the same equilibrium state from opposite directions, both the experiments and DNS confirm that complete equilibration is achieved within the run time to a high level of accuracy. From DNS, running averages over intervals of 100 s ($\delta\hat{t}_D \approx 4 \times 10^{-4}$) show that the net boundary heat flux (figure 11) eventually vanishes

https://doi.org/10.1017/jfm.2013.244 Published online by Cambridge University Press

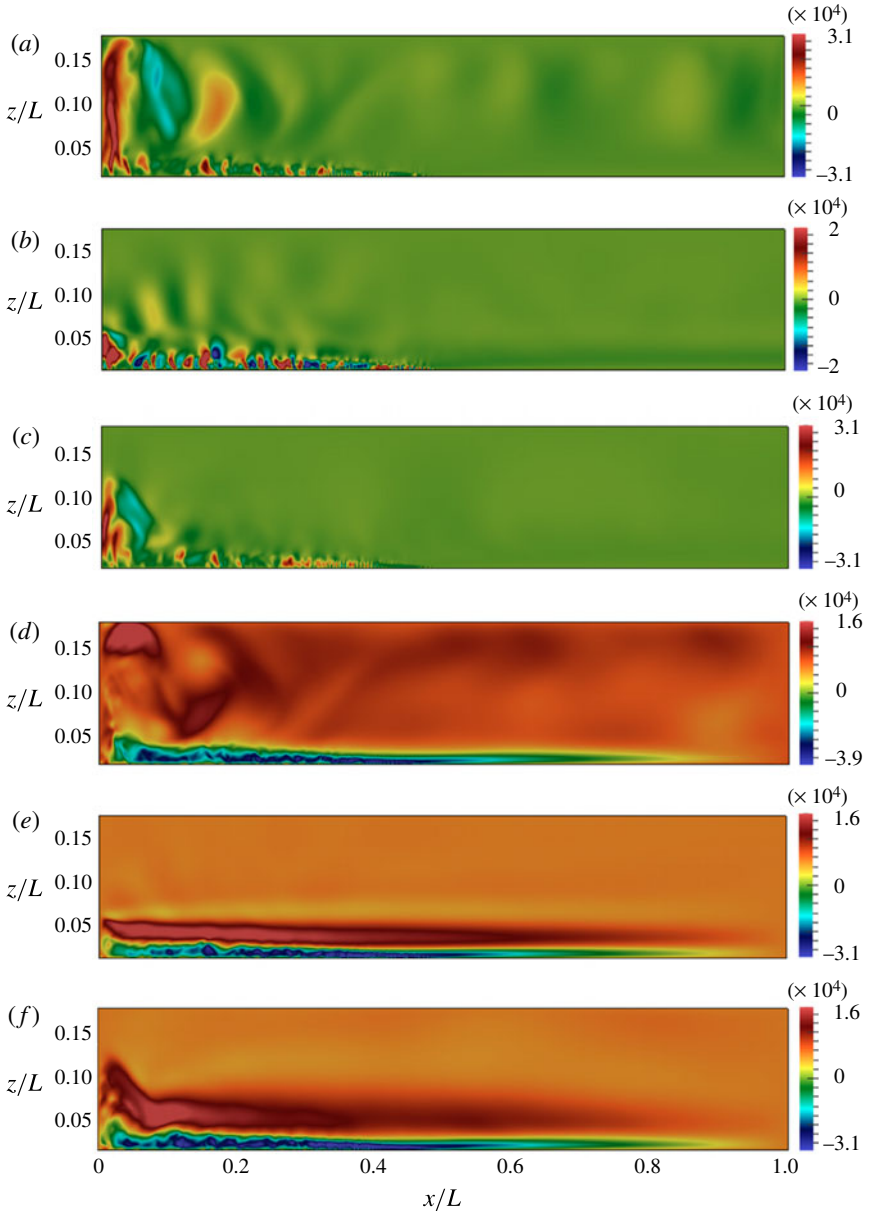


FIGURE 13. Snapshots of velocity components from DNS for the cooling adjustment after T_H is decreased (DNSc in table 1): (*a–c*) vertical velocity $\hat{w}$; (*d–f*) horizontal velocity $\hat{u}$; (*a,d*) from the initial equilibrium state; (*b,e*) at $\hat{t}_D = 0.095$ after the perturbation; (*c,f*) at $\hat{t}_D = 0.8$. Velocities are scaled by κ/L and colour scales are shifted as the flow evolves.

to within 0.1 % of the total heat transport. In the experiments the time-averaged equilibrium temperatures (for a given sensor) are found to within $10^{-3}\Delta T$, where the primary practical limitations are posed by the natural fluctuations in the equilibrium state and ambient room temperature fluctuations. The uncertainty in measured time scales, estimated from differences between similar runs, is 10–15 %.

https://doi.org/10.1017/jfm.2013.244 Published online by Cambridge University Press

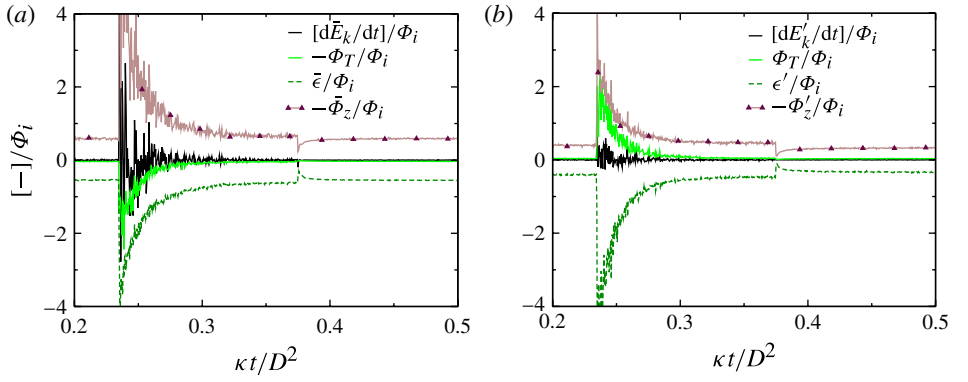


FIGURE 14. (Colour online) Evolution of (*a*) mean and (*b*) turbulent mechanical energy conversion rates, each integrated over the entire volume of the box and normalized by $\Phi_i = 5.5 \times 10^{10}(\rho_0\kappa^3/L)$, the time-averaged generation of background potential energy by molecular diffusion down the mean density gradient evaluated in the final equilibrium state. Quantities are the total rate of change of mean and turbulence kinetic energy ($\mathrm{d}\bar{E}_k/\mathrm{d}t$, $\mathrm{d}E'_k/\mathrm{d}t$), net generation of mean E_k and turbulence E'_k kinetic energy by buoyancy fluxes ($-\bar{\Phi}_z$, $-\Phi'_z$), loss of mean E_k to turbulence E'_k (Φ_T) and viscous dissipation of mean and turbulence kinetic energy ($\bar{\epsilon}$, ϵ'). As indicated by the time axis, the plot begins with the first equilibrated convection state in figure 10 and shows adjustment to the subsequent warming perturbation and the later cooling perturbation.

For destabilizing (warming) boundary perturbations the evolution of each of the transient flows is well described by a single exponential function throughout at least 95 % of the adjustment, after which internal fluctuations in the flow make the mean trend increasingly uncertain. In some experiments the exponential behaviour was demonstrated through 99 % of the adjustment. The DNS shows a small additional slowing of the temperature adjustment with time (the curvature seen in figure 10*c*). Stabilizing (cooling) perturbations lead to more complicated behaviour (figure 10*d*). We therefore evaluate the times τ_e and τ_{95} at which the temperature adjustment is $1/e$ (63.2 %, $\Theta = 0.368$) and 95 % ($\Theta = 0.05$) complete, respectively. For each location in the flow the two times serve as indicators of the accuracy of a single exponential description and of the differences between early and late stages of the evolution. These times (normalized by D^2/κ) are collated in figures 15 and 16 for cases giving net warming with imposed flux and temperature difference, respectively, and in figures 17 and 18 for cases giving net cooling, again with imposed flux and temperature difference, respectively. Each of these plots includes the results for perturbations to each of the heating and cooling regions of the boundary, and shows data (grouped in pairs) from two measurement locations that represent the top of the box and the lower region of the interior just outside the boundary layer. The predicted time scales (2.10) or (2.19) for the warming cases are also indicated on the relevant plots, whereas the calculated conduction time through a deep stagnant layer is shown against the results for cooling perturbations.

For a fixed heating power Q (figure 15) the temperature at all levels in the box initially responded to an increase in the cooling temperature (on the left of each chart) on the e-folding time $\tau_e = 0.075D^2/\kappa$, a value 25 % smaller than that predicted ($\kappa\tau_F/D^2 \approx 0.10$, using $c_2 = 2.7$ and $\beta = 1.4$ in 2.10). The response to an increase in Q (on the right of each chart) shows slightly longer times and is in close agreement with

https://doi.org/10.1017/jfm.2013.244 Published online by Cambridge University Press

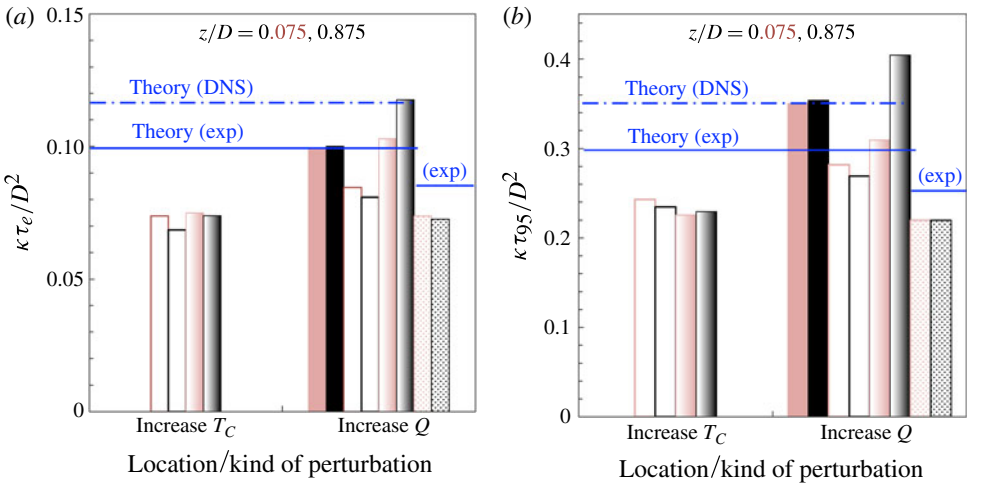


FIGURE 15. (Colour online) Adjustment times (*a*) τ_e and(*b*) τ_{95} for interior temperatures to reach $\Theta = 1/e$ and $\Theta = 0.05$, respectively, in cases with imposed heating power Q (flux F) and perturbations leading to a warming of the box. Times are normalized by κ/D^2. On the left are results for an increase in the cooling temperature T_C; on the right are the times found for an increase in heating flux. All results are shown as pairs for $z/D = 0.075$ (grey, shown in brown online) and $z/D = 0.875$ (black). Bar shading indicates DNS (solid fill), experiments with low ambient room temperature (open bars), experiments with matched room temperature and 'standard' value of Q (graded shading), and experiments with doubled heat flux (stippled). In (*a*) the horizontal solid line is the predicted time scale τ_F (2.10) for the experiments with the standard Q (or with double Q on the right), and the dash–dot line is the predicted τ_F for the DNS Rayleigh number. In (*b*) the lines are as in (*a*) but multiplied by $-\ln(0.05) = 3.0$.

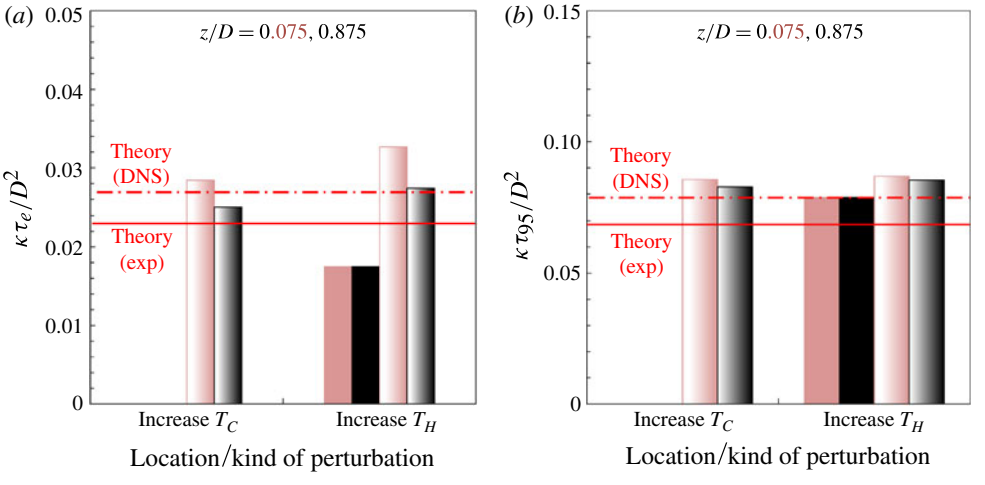


FIGURE 16. (Colour online) Adjustment times (*a*) τ_e and (*b*) τ_{95} in cases with imposed temperature difference ΔT and warming perturbations. Note the time axis scales are 1/3 those in figure 15. Shading as in figure 15 but for runs with imposed ΔT. In (*a*) the horizontal lines are the predicted time scale τ_Δ (2.19) for the Rayleigh number of the experiments (solid) and the DNS (dash-dot). Lines in (*b*) are these predictions multiplied by $-\ln(0.05) = 3.0$.

https://doi.org/10.1017/jfm.2013.244 Published online by Cambridge University Press

the prediction. The results with a room temperature 6 °C cooler than the box show a slightly smaller adjustment time. The experiment forced by double the applied power input (experiment 10, table 1) showed a time scale approximately 40 % smaller than that for the 'standard' Rayleigh number, consistent with the predicted Rayleigh number dependence (indicated by the horizontal lines) after allowing for greater sidewall heat loss from the hotter box. The adjustments reached 95 % completion (figure 15*b*) at a time that is close to three times longer than τ_e, as is expected for a simple exponential evolution throughout the adjustment. The DNS for an increase in Q shows an e-folding time 15 % smaller than the model prediction and a τ_{95} in exact agreement with the prediction (where the slightly smaller Rayleigh number in the DNS increases the predicted time scale by 17 % relative to the experimental conditions). Overall, the key results for warming under an applied flux are e-folding times $\kappa\tau_e/D^2 \approx \kappa\tau_F/D^2 \approx 0.1$, as predicted, with little dependence on the location of the perturbation.

For destabilizing boundary perturbations with an imposed temperature difference (figure 16) the time scales were all substantially smaller than in the corresponding runs with applied flux. They also showed no dependence on the location of the perturbation (an increase in T_C or T_H) and no dependence on position in the box. The experiments give $\tau_e = 2.6 \times 10^{-2} D^2/\kappa$ and $\tau_{95} = 8 \times 10^{-2} D^2/\kappa$. The corresponding DNS results for an increase in T_H (from both the first and second equilibrations in figure 10) are $\tau_e = 1.75 \times 10^{-2} D^2/\kappa$ and $\tau_{95} = 7.9 \times 10^{-2} D^2/\kappa$. These times are all in agreement with the prediction (2.19) that applied temperature boundary conditions give relatively rapid equilibration as a consequence of convective transport from the bottom boundary. The DNS gives the shortest time, consistent with the earlier observation that the solution has an interior temperature $\hat{T}_{top}$ that is closer to the heating boundary temperature than is the case in the experiments.

The ratio of the e-folding time scales τ_e in applied temperature runs to those in the corresponding applied flux cases is 0.25–0.37 from the experiments and 0.18 from the DNS. The corresponding ratios of τ_{95} are 0.21–0.37 from experiments and 0.22 from DNS. These results are in close agreement with the prediction (2.21) $\tau_\Delta/\tau_F \approx 0.22$.

The adjustment times for cooling boundary perturbations are summarized in figures 17 and 18 for applied Q and applied ΔT, respectively. The overarching result is that the normalized equilibration time scales for cooling are in every case longer, up to seven times, compared with adjustments following the same kind of perturbation of the opposite sign. There is little difference (a factor of 1–1.3) between responses to positive and negative perturbations when changing the imposed heating flux (table 1, runs 5 and 6), despite the obvious differences already described in the nature of the transient circulation patterns. The time scales following a decrease in the cooling temperature T_C under an applied ΔT are a factor of 2–2.4 longer than for an increase in T_C (table 1, runs 12 and 13). However, larger differences are found for changes in the cooling temperature under an applied heating power Q, and for perturbations in heating temperature under an applied temperature difference. Specifically, equilibration time scales are approximately 3.4 times longer for a decrease (compared to an increase) in cooling temperature T_C under an applied heating flux (table 1, runs 7 and 9; left-hand side of each panel in figures 15 and 17). The greatest contrast of all is found between the stabilizing and destabilizing perturbations in T_H under an applied ΔT (table 1, runs 14 and 15; right-hand side of each panel in figures 16 and 18): here $\kappa\tau_e/D^2$ is a factor of 7.1, and $\kappa\tau_{95}/D^2$ a factor of 6.6, larger for the cooling case. This latter contrast is confirmed by the sole cooling run attempted with DNS (table 1, DNSc), which gives $\kappa\tau_e/D^2$ approximately 12 times, and $\kappa\tau_{95}/D^2$ near 9.5 times, longer than those for an increase in T_H (DNSb).

https://doi.org/10.1017/jfm.2013.244 Published online by Cambridge University Press

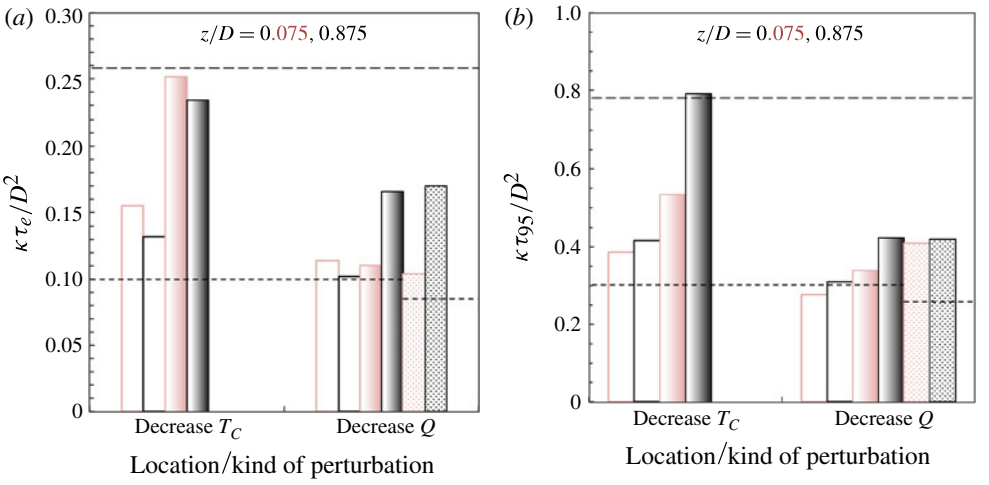


FIGURE 17. (Colour online) Adjustment times (*a*) τ_e and (*b*) τ_{95} for temperatures in cases with imposed heating power Q and cooling perturbations. All results are shown as pairs for $z/D = 0.075$ (grey, shown in brown online) and $z/D = 0.875$ (black). On the left are results for an decrease in the cooling temperature T_C; on the right are the times found for a decrease in heating flux. Times are normalized by κ/D^2. Bar shading indicates experiments with low ambient room temperature (open bars), experiments with matched room temperature and 'standard' value of Q (graded shading), and experiments with doubled heat flux (stippled). The horizontal dashed line shows the calculated e-folding time (2.22) (in *a*) and time for 95 % (in *b*) for the case of temperature change by conduction in stationary water through a depth $d = 0.8D$. The horizontal dotted line is the time scale τ_F (in *a*) and $3.0\tau_F$ (in *b*) predicted for warming cases, and is shown here only as a reference.

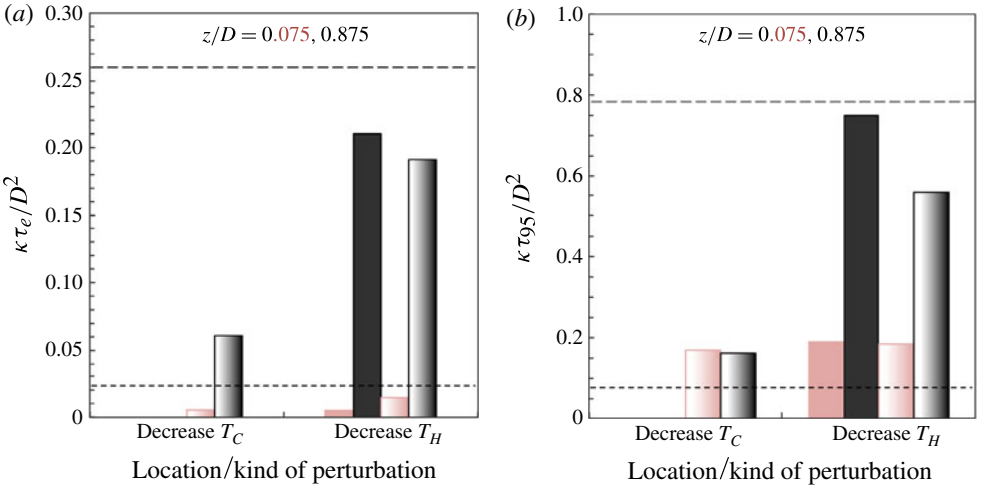


FIGURE 18. (Colour online) Adjustment times (*a*) τ_e and (*b*) τ_{95} in cases with imposed temperature difference ΔT and perturbations leading to a cooling of the box. Colours and shading as in figure 17: DNS (solid fill) and experiments (graded shading). The dashed line shows the calculated time for conduction (2.22) through a depth $d = 0.8D$, the dotted line is the predicted time scale τ_Δ (2.19) for warming cases, shown here only as a reference.

https://doi.org/10.1017/jfm.2013.244 Published online by Cambridge University Press

For most classes of cooling boundary perturbation there is a significant difference between the adjustments at locations near the boundary layer and those near the top of the box, indicating the increased stable stratification. The difference is most obvious in the e-folding times, owing to the rapid formation of the shallow circulation cell in the lower 15–20 % of the box (and which encompasses the lower measuring position at $z/D = 0.075$ immediately after the boundary perturbation). This difference is particularly large for applied ΔT (figure 18), where the shallow cell forms most quickly and is forced to cool most rapidly, as the shallow circulation approaches an equilibrium with the new values of T_C or T_H. Applying the analytical equilibration model for a uniform layer (2.10) to the shallow cell alone, using the observed cell depth ($\approx 3h$), neglecting the heat gain from the stagnant water above, and treating this cell as a case of horizontal convection at smaller Rayleigh number, suggests an adjustment time scale for the shallow cell alone of $\kappa\tau_e/D^2 \sim 0.8(h/D)^2 \approx 4 \times 10^{-3}$. The DNS result at $z/D = 0.075$ (figure 18*a*) shows a cooling rate consistent with this estimate, at $\kappa\tau_e/D^2 = 4.8 \times 10^{-3}$.

In contrast the overlying, nearly stagnant layer in cooling adjustments cools relatively slowly. The largest normalized values of τ_{95} at the top of the box are found for a decrease in the cooling temperature with applied heating flux, or a decrease in the heating temperature with applied ΔT, both giving $\kappa\tau_{95}/D^2 \approx 0.2$. As shown in figures 17 and 18, these longest equilibration times are close to the calculated time taken for conduction of heat, through a rigid slab of water of thickness $d = 0.8D$, to adjust the temperature at the top of the box through 95 % of the total change. At large times the whole of the box, including the lower circulation cell, adjusts on the slow time scale. This is further illustrated by the large time adjustment of the boundary heat flux imbalance (figure 11).

The rate of cooling in the upper regions, again for applied ΔT (figure 18), is three times faster when the boundary perturbation is a decrease of the cooling temperature T_C rather than of the heating temperature T_H. This reflects the strong role of small-scale convection within the boundary layer at the heating boundary and the resulting tighter linkage of plume and interior temperatures to T_H rather than T_C. Thus, when T_H is decreased, the plume temperature is decreased (relative to the initial interior temperature) in line with the boundary perturbation and the plume convection is strongly suppressed. When T_C is decreased, the boundary layer reaches essentially the same maximum temperature at the heating region by the time it enters the plume, the plume is only weakly suppressed, and the recovery of deep convection is faster. This more rapid adjustment is consistent with the observations of a more active plume or penetrative fountain, including greater fluctuations, earlier penetration to the top of the box, and more entrainment from the nearly stagnant upper region. This also explains why the cooling times following a decrease of T_C were only double those for the fastest warming adjustments. A decrease in the heating flux, on the other hand, does not force such a rapid increase of boundary layer density as applied temperatures and therefore the box does not become as stably stratified, and the transient bottom circulation cell is not as shallow.

The effects of sidewall heat loss in the experiments can be assessed from a comparison of experiments at different room temperatures and different time scales. The comparison is made only for imposed flux cases (where it is expected to be greatest) and shows that the greater temperature difference does not lead to a significant difference in those experiments which approached thermal equilibrium relatively quickly. We conclude that heat loss is unimportant for all of the experiments

https://doi.org/10.1017/jfm.2013.244 Published online by Cambridge University Press

with a closely matched room temperature, with the possible exception of the case of a decreased cooling temperature and applied flux.

7. Conclusions

Perturbations to the boundary conditions in thermally equilibrated horizontal convection break the delicate flow balance that gives zero net heat flux through every level in the flow. The dramatic response of the circulation following a boundary perturbation attests to the fine nature of this balance. The transient net buoyancy flux following boundary perturbations that lead to a destabilizing net heat flux (a net warming in the case of basal forcing) produces an immediate and relatively very large increase in the circulation, with little dependence on whether the change is imposed at the cooling or the heating region of the boundary. DNS reveal that a 10 % increase in the boundary temperature in the heating region leads to a 10-fold increase in the maximum rate of production of mean kinetic energy by buoyancy fluxes. Stabilizing perturbations (a net cooling for basal forcing) temporarily increase stratification, greatly weaken the convection and confine circulation to a shallow cell.

The adjustment of the convective circulation toward a new equilibrium state has been used to reveal the dominant mechanisms of vertical transport. In net warming cases the evolution to the new equilibrium is close to exponential, which implies that the adjustment is governed throughout by the same processes. The time scales in these cases are consistent with the hypothesis that the net rate of heat input is governed by mechanisms within the thin boundary layer (and the total heat capacity of the domain) with no significant role for diffusion through the interior. There are two different time scales for warming equilibrations at the large Rayleigh number used here. For applied heat input flux the time scale indicates that the net rate of warming of the box is controlled by the rate of heat withdrawn via conduction in the stable boundary layer over the cooling area of the boundary. For applied temperature difference, irrespective of whether it is the cooling or heating temperature that is increased, the net rate of warming of the box is instead controlled by convective transfer from the heated portion of the boundary. Thermal equilibration is complete at times that are much less than the time required by conduction through the depth of the box. Equilibration to the final equilibrium state (which could be monitored through 99 % of the adjustment in both experiments and DNS) revealed no evidence of a slower time scale, and equilibration from both higher and lower initial interior temperatures confirms that the same equilibrium state was achieved.

Perturbations leading to net cooling of the box, on the other hand, almost immediately confine the circulation to a shallow cell against the forcing boundary and there is a very short time scale for temperature change in the shallow cell. The adjustment times for cooling of the whole domain are variable, depending on the kind of boundary conditions and the location of the perturbation. A reduction of the cooling boundary temperature under an applied flux, or a reduction of the heating temperature, both give time scales that are comparable with that for conduction through the depth of the box. However, stabilizing perturbations at the heating portion of the base with applied flux, or at the cooling end with applied temperature difference, lead to much shorter time scales because the cooling adjustment is supported by the endwall plume, which in turn is closely linked to the small-scale convective heat transfer above the heated portion of the boundary. For the practically available range of perturbation amplitudes (down to 2.4 % of the total forcing temperature difference) the experiments

https://doi.org/10.1017/jfm.2013.244 Published online by Cambridge University Press

show no evidence of a threshold in the perturbation amplitude required for the plume convection to 'shut down'.

The results may have important implications in oceanography. In particular, equilibration time scales much less than D^2/κ and the conclusion that boundary-layer processes govern the convective circulation are at odds with the widespread view that the ocean meridional overturning circulation is governed by the rate of vertical diffusive transport in the abyssal water (Munk 1966; Wunsch & Ferrari 2004). In that view, vertical diffusion of density maintains the abyssal stratification in the presence of an upward mean advection in the interior. (Note that the diffusive transport in the oceans is a result of small-scale turbulent mixing, which has a large-scale separation from the circulation and, at least in terms of its effects on the momentum and buoyancy budgets, simply acts as an enhanced molecular diffusion of heat and buoyancy.) In contrast the present results for imposed boundary temperatures indicate an equilibration time scale of the order of $0.01D^2/\kappa$ (or around 10^3 years, taking an average depth of 4000 m and average measured turbulent diffusivity of the order of 10^{-5} m^2 s^{-1}), which implies that abyssal diffusion is unimportant for vertical density transport; instead the transport is dominated by the boundary-layer mechanisms responsible for the loss of buoyancy from the ocean surface and, in the interior, by vertical advection of interior water upon being entrained into the high-latitude regions of sinking dense water (Hughes & Griffiths 2006). This advective transport pathway is fundamentally different to and much more rapid than a diffusive pathway through the abyssal depths. Consistent with this result is the ratio of the time scale for vertical advection through the ocean depth, or ventilation time ($\sim 10^3$ years, as commonly estimated from the rate of production of dense bottom water), and the time scale for turbulent diffusion through the ocean depth ($\sim 10^5$ years, based on $\kappa \sim 10^{-5}$ m^2 s^{-1}).

Hence, we predict that turbulent mixing and diffusion in the interior can play a substantial role only in slowly re-establishing deep circulation following perturbations that cause a shutdown of deep sinking at high latitude. In equilibrium, the deep interior stratification of the oceans would be maintained primarily by the vertical convergence (associated with the horizontal entrainment) of vertical velocity as water is displaced upwards by the production (in the plume) of new bottom water (Hughes & Griffiths 2006; Stewart *et al.* 2012). Although considering different dynamics, a negligible role for abyssal diffusion is consistent with the thesis that upwelling of deep waters in the Southern Ocean due to Ekman pumping imply a reduced, even minimal, dynamical role of abyssal mixing (Marshall & Speer 2012).

We further conclude that the ocean response to many classes of change in the surface (buoyancy) boundary conditions, at least in a buoyancy-forced overturning, will be governed by processes within the upper boundary layer. Our results suggest that under some circumstances the dominant control would be (turbulent) diffusion through the boundary layer, or thermocline, at low latitudes: this includes the case of a decrease in imposed heat input flux at low latitudes. In other cases the response would be governed by vertical, convective transfer of buoyancy within the surface mixed layer at high latitudes, which leads to the most rapid adjustments: this is relevant when a decrease in the surface buoyancy (a densification by increased cooling or increased salinity) is imposed at either high or low latitude. An unexpected result is a short time scale of adjustment for imposed temperatures following a stabilizing boundary perturbation (decreased imposed surface density) at low latitudes: despite a transient shut-down of deep convection the density of surface water at high latitudes in this case tends to be maintained by the surface condition. Thus, the present results highlight the

https://doi.org/10.1017/jfm.2013.244 Published online by Cambridge University Press

role of the ocean mixed layer and the importance of mixed layer parameterizations in ocean models.

We note that the boundary condition changes to which the global ocean circulation must respond include phases of global cooling and global warming in glacial cycles having periods of 20 000–100 000 years, shorter millennial to decadal climate oscillations and anthropogenic global warming on decadal time scales. Naturally these changes are far more complex than the simple, idealized boundary perturbations examined here. We also note that the ocean boundary conditions are generally modelled by a prescribed surface temperature (modified by a short relaxation time). However, the actual boundary conditions are complex: the low-latitude stabilizing buoyancy input might instead be approximated as a prescribed flux (due to solar insolation and evaporation, with no direct control on surface temperature) and the high-latitude cooling condition is close to prescribed temperature (constrained by the freezing temperature) but complicated by surface freshwater inflow.

A relevant boundary condition that could not be examined in the present apparatus is an imposed flux at the stabilizing region of the boundary. In that case the flow responses to boundary perturbations (of either sign and in either location on the boundary) are expected to again depend on the class of perturbation, with fastest adjustments likely in cases where the destabilizing boundary temperature is either constant or is increased. In the present experiments it was also impractical to further increase the Rayleigh number and the molecular diffusivity could not be varied. Useful future investigations would be to examine transient flows in salinity-driven convection, in which Rayleigh numbers well beyond those practical with DNS or thermal convection can be achieved, and to examine transient adjustment in the presence of added small-scale mechanical mixing (used previously to examine equilibrium states; see, for example, Whitehead & Wang 2008; Stewart *et al.* 2012), which would allow both the rate and spatial distribution of diffusivity to be varied.

Acknowledgements

We thank T. Beasley for construction and assistance with the laboratory experiments. This work was funded by the Australian Research Council (DP1094542 and DP120102744), and the numerical simulations were supported by time allocation on the National Computing Infrastructure at The Australian National University. G.O.H. was supported by an ARC Future Fellowship (FT100100869). Research Interns K. Burke, R. Holmes, S. Jaspers and C. Wong assisted in the experimental program.

Supplementary movies

Supplementary movies are available at http://dx.doi.org/10.1017/jfm.2013.244.

REFERENCES

BOROWSKI, D., GERDES, R. & OLBERS, D. 2002 Thermohaline and wind forcing of a circumpolar channel with blocked geostrophic contours. *J. Phys. Oceanogr.* **32**, 2520–2539.

CARSLAW, H. S. & JAEGER, J. C. 1959 *Conduction of Heat in Solids*. Oxford University Press.

CHIU-WEBSTER, S., HINCH, E. J. & LISTER, J. R. 2008 Very viscous horizontal convection. *J. Fluid Mech.* **611**, 395–426.

COMAN, M. A., GRIFFITHS, R. W. & HUGHES, G. O. 2010 The sensitivity of convection from a horizontal boundary to the distribution of heating. *J. Fluid Mech.* **647**, 71–90.

GANOPOLSKI, A. & RAHMSTORF, S. 2001 Rapid changes of glacial climate simulated in a coupled climate model. *Nature* **409**, 153–158.

https://doi.org/10.1017/jfm.2013.244 Published online by Cambridge University Press

GAYEN, B., GRIFFITHS, R. W., HUGHES, G. O. & SAENZ, J. A. 2013 Energetics of horizontal convection. *J. Fluid Mech.* **716**, R10.

GRIFFITHS, R. W., MAHER, N. & HUGHES, G. O. 2011 Horizontal convection under oscillatory buoyancy forcing. *J. Mar. Res.* **69**, 523–543.

HOGG, A. MCC. 2010 An antarctic circumpolar current driven by surface buoyancy forcing. *Geophys. Res. Lett.* **37**, L23601.

HUGHES, G. O. & GRIFFITHS, R. W. 2006 A simple convective model of the global overturning circulation, including effects of entrainment into sinking regions. *Ocean Model.* **12**, 46–79.

HUGHES, G. O. & GRIFFITHS, R. W. 2008 Horizontal convection. *Annu. Rev. Fluid Mech.* **40**, 185–208.

HUGHES, G. O., GRIFFITHS, R. W., MULLARNEY, J. C. & PETERSON, W. H. 2007 A theoretical model for horizontal convection at high Rayleigh number. *J. Fluid Mech.* **581**, 251–276.

HUGHES, G. O., HOGG, A. MCC. & GRIFFITHS, R. W. 2009 Available potential energy and irreversible mixing in the meridional overturning circulation. *J. Phys. Oceanogr.* **39**, 3130–3146.

MARSHALL, J. & SPEER, K. 2012 Closure of the meridional overturning circulation through southern ocean upwelling. *Nat. Geosci.* **5**, 171–180.

MORI, A. & NIINO, H. 2002 Time evolution of nonlinear horizontal convection: its flow regimes and self-similar solutions. *J. Atmos. Sci.* **59**, 1841–1856.

MULLARNEY, J. C., GRIFFITHS, R. W. & HUGHES, G. O. 2004 Convection driven by differential heating at a horizontal boundary. *J. Fluid Mech.* **516**, 181–209.

MUNK, W. H. 1966 Abyssal recipes. *Deep-Sea Res.* **13**, 707–730.

PIERCE, D. W. & RHINES, P. B. 1996 Convective building of a pycnocline: laboratory experiments. *J. Phys. Oceanogr.* **26**, 176–190.

ROSSBY, H. T. 1965 On thermal convection driven by non-uniform heating from below: an experimental study. *Deep-Sea Res.* **12**, 9–16.

ROSSBY, H. T. 1998 Numerical experiments with a fluid non-uniformly heated from below. *Tellus* **50**, 242–257.

SAENZ, J., HOGG, A. MCC., HUGHES, G. O. & GRIFFITHS, R. W. 2012 Mechanical power input from buoyancy and wind to the circulation in an ocean model. *Geophys. Res. Lett.* **39**, L13605.

SCOTTI, A. & WHITE, B. 2011 Is horizontal convection really non-turbulent? *Geophys. Res. Lett.* **38**, L21609.

STEVENS, R. J. A. M., VERZICCO, R. & LOHSE, D. 2010 Radial boundary layer structure and Nusselt number in Rayleigh–Bénard convection. *J. Fluid Mech.* **643**, 495–507.

STEWART, K. D., HUGHES, G. O. & GRIFFITHS, R. W. 2011 When do marginal seas and topographic sills modify the ocean density structure? *J. Geophys. Res.* **116**, C08021.

STEWART, K., HUGHES, G. O. & GRIFFITHS, R. W. 2012 The role of turbulent mixing in an overturning circulation maintained by surface buoyancy forcing. *J. Phys. Oceanogr.* **42**, 1907–1922.

STOMMEL, H. 1962 On the smallness of sinking regions in the ocean. *Proc. Natl Acad. Sci. Washington* **48**, 766–772.

WANG, W. & HUANG, R. X. 2005 An experimental study on thermal convection driven by horizontal differential heating. *J. Fluid Mech.* **540**, 49–73.

WHITEHEAD, J. A. & WANG, W. 2008 A laboratory model of vertical ocean circulation driven by mixing. *J. Phys. Oceanogr.* **38**, 1091–1106.

WUNSCH, C. & FERRARI, R. 2004 Vertical mixing, energy, and the general circulation of the oceans. *Annu. Rev. Fluid Mech.* **36**, 281–314.

https://doi.org/10.1017/jfm.2013.244 Published online by Cambridge University Press